Design of Synthetic Jet Actuators for Jet Noise Control

Towards Aircraft Noise Reduction

MSc Thesis

Emmanouil Vretoudakis

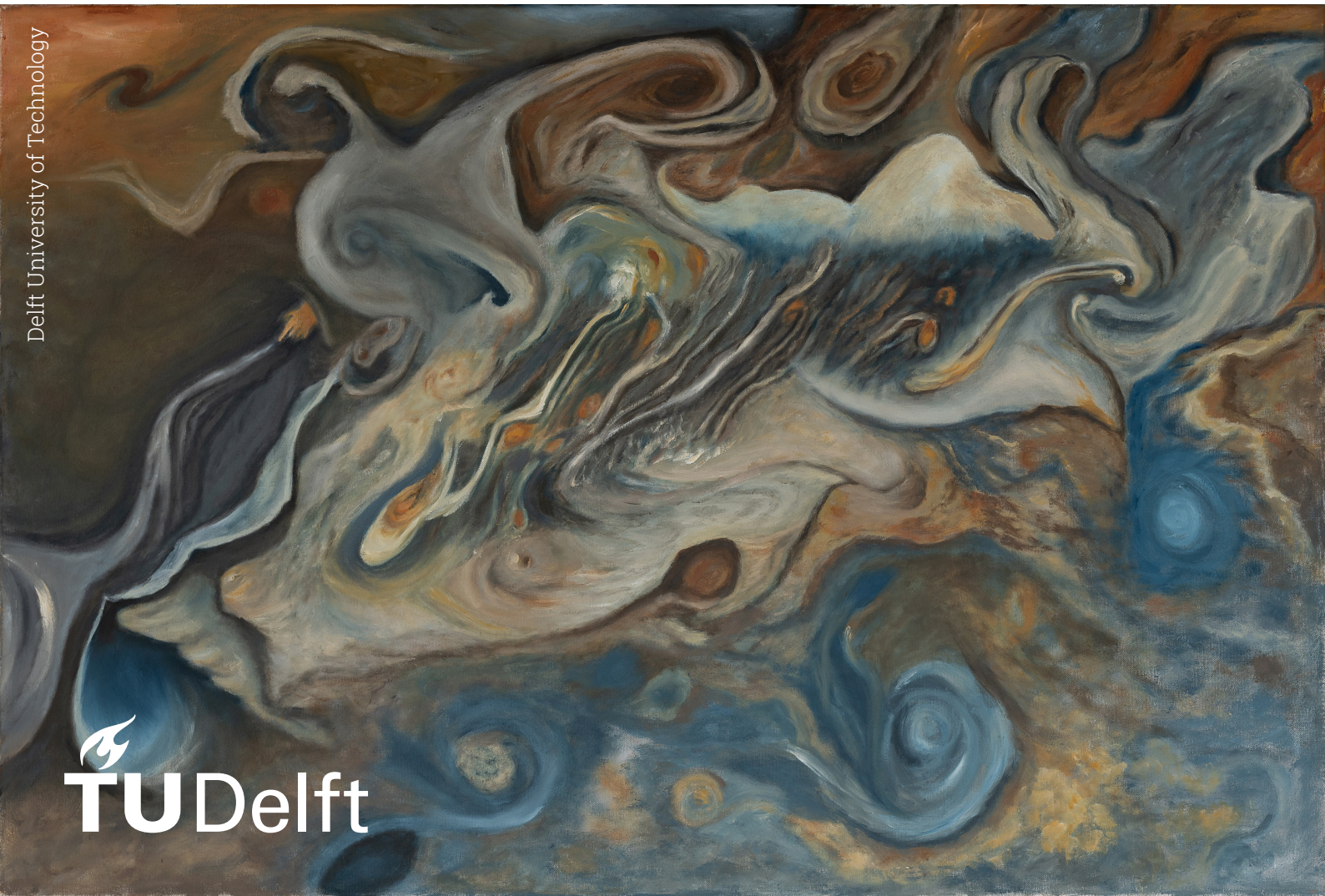

Delft University of Technology

TU Delft

Design of Synthetic Jet Actuators for Jet Noise Control

Towards Aircraft Noise Reduction

by

Emmanouil Vretoudakis

Student Name	Student Number
Emmanouil Vretoudakis	4799216

Instructors:	D. Ragni, M. Raiola
Project Duration:	September, 2023 - August, 2024
Faculty:	Faculty of Aerospace Engineering, Delft

Cover painting: Πλανήτης Δίας (Planet Jupiter) by Maria Stratidaki

TU Delft

Preface

The current thesis is submitted in partial fulfillment of the requirements for the degree of Master of Science in Aerodynamics at the Technical University of Delft. The research presented herein was conducted in the experimental facilities of University Carlos III of Madrid in Leganes, under the guidance of Daniele Ragni from the Department of Wind Energy of TU Delft as well as Marco Raiola from the Aerospace Engineering department of UC3M. The thesis focuses on turbulent jet noise analysis and control using synthetic jet actuators.

The study aims to contribute to the ongoing advancements in understanding turbulent jet noise creation mechanisms, studied in the context of active flow control. The work builds on both theoretical foundations and experiments, integrating theoretical aeroacoustic modelling for jet noise prediction to the design of synthetic jet actuator geometries for practical control.

At this point I would like to express gratitude to my supervisors Daniele and Marco not only for the opportunity to have such an interesting project outside of TU Delft, but also for their guidance, insights and encouragement throughout the length of this project. I have to give a special thank you to Luca Franceschelli for the constant guidance all the way from the literature study till the final experiments and for the patience he showed while teaching me the various methods. Of course the experience would not be as enjoyable as it was if my roommates and friends from Madrid and Delft were not there for me therefore I would like to thank everyone for the fun times we had and will have together in the future. Special admiration to my childhood friend Kiamouris for the large contribution to my phone bill which reminded me how important good people are in our lives. Finally a massive “Ευχαριστώ” to my family Ioannis, Sylvia and Dafni in Greece who helped me be confident in my decisions and were there for me in the good and in the bad.

I hope this thesis provides valuable insights into the complexities of jet aeroacoustics and contributes to the broader field of aerodynamics.

Emmanouil Vretoudakis
Delft, September 2024

Abstract

This thesis investigates the turbulent jet aeroacoustic phenomena and explores the potential of active flow control using synthetic jet actuators to mitigate noise emissions. The study initially focuses on the development and validation of a comprehensive noise-source prediction model that combines already existing theoretical jet aeroacoustics formulas into an iterative solver that utilises existing jet farfield noise data. The thesis then continues with the goal of designing a synthetic jet actuator to be used as active flow control in the jet that aims to contribute to the emitted noise mitigation.

The research begins by analysing the literature revolving around aeroacoustics of jets in general and the efforts to locate and characterise the noise sources in the wake of the jet in specific. The aeroacoustic analogies created for jet noise emissions are reviewed and later on form the basis of the predictive model. The core of this first part of the work involves the integration of the aforementioned analogies in the form of analytical formulas for farfield noise calculation into the modelling framework that incorporates the already existing farfield noise data for the various jets. These noise data are used as the target within a loss function that aims for the convergence of the predicted farfield noise to the experimental one. The characterisation of the noise sources within the jet are then a product of this iterative solving and take the form of energy/frequency requirements. This framework is applied to various jet configurations resulting in a global guide of velocity/frequency requirements for effective actuation of subsonic jets. The major output of the model is regarding a Mach 0.5 jet for which the requirement for effective actuation was to introduce disturbances with an amplitude of 15m/s at the frequency range from 600 to 800Hz.

Focus is then given on potential active flow control methods that take the outputs of the noise-source prediction model and are able to provide the specific energy requirement at the required frequency range. Given the Mach 0.5 jet, synthetic jet actuators are chosen as the type of actuation and the research henceforth continuous with the modelling of actuators as a coupled resonator system. Once more, the outcomes of this modelling point at a specific actuator geometry which sparks the design, manufacturing and testing of said actuator. The designed piezoelectric-driven synthetic jet actuator was found to provide the 15m/s requirement at the frequency range of 700 to 900Hz which is deemed sufficient. The report finally discusses the practical implications of these findings in an effort to construct and evaluate an active flow control demonstration using the aforementioned actuators on an actual jet while also putting everything into context for future aeroacoustic modelling and aerospace applications.

This work contributes to the ongoing efforts in reducing noise pollution in aerospace environments and provides a foundation for future research in active flow control technologies. The methodologies developed and the results obtained are expected to have broader applications in the design and optimization of quieter, more efficient aircraft.

[Keywords: Turbulent Jet, Aeroacoustics, Jet Noise, Active Flow Control, Synthetic Jet Actuators]

Contents

List of Figures

List of Tables

1

Introduction

1.1. The Jet Noise Problem

Aircraft jet noise has posed a significant environmental challenge since the commercialization of jet engines. Rapid advancements in aviation technology brought about powerful jet engines that improved air travel's efficiency and speed but at a cost—increased noise pollution. This issue has grown with the global expansion of airports and increased flight frequencies, affecting millions worldwide. Noise from aircraft, particularly during takeoff and landing, has been a critical concern for communities near airports due to its adverse effects on health and quality of life [39].

The journey to mitigate jet noise began during the 1950s and 1960s with the advent of turbojet engines, which were significantly noisier. This period marked the initiation of focused efforts to reduce noise through engine design improvements and operational strategies. The introduction of turbofan engines, which utilized high bypass ratios, significantly advanced these efforts. Engines such as the General Electric GE-90 exemplified this technology, which not only enhanced fuel efficiency but also crucially reduced noise levels by decreasing the velocity and temperature of the jet exhaust [26].

Contemporary developments continue to build on past achievements with innovations like quieter engine technologies and refined aerodynamic designs to minimize noise at the source. Regulatory bodies, including the International Civil Aviation Organization (ICAO), play a pivotal role by setting and updating noise standards, pushing for quieter aircraft through technological mandates. As a result, modern aircraft are approximately 75% quieter than those from several decades ago. Despite these advancements, aircraft noise remains a significant issue, primarily due to the increasing frequency of flights and more extensive airport operations [39].

The significance of the aircraft noise problem extends beyond discomfort. Studies have linked prolonged exposure to aircraft noise with increased risks of cardiovascular diseases, sleep disturbance, and diminished mental health. The World Health Organization has categorized environmental noise as a major threat to public health, second only to air pollution [32] [39].

Efforts to manage and mitigate jet noise are therefore crucial not only for complying with regulatory limits but also for enhancing the quality of life for affected populations. Studies suggest that even moderate reductions in noise levels can significantly improve health outcomes and community satisfaction [39].

A typical distribution of the aircraft noise sources upon take-off can be seen in Figure 1.1 (data acquired from 2013). It can be clearly seen how the total aircraft noise is dominated by that of the engine which is in turn dominated by the noise produced by the jet of the engine.

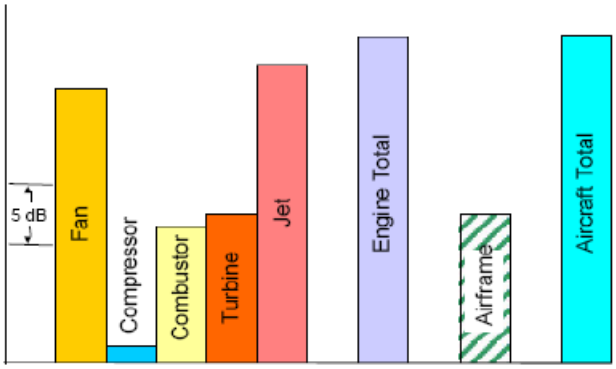

Figure 1.1: Typical aircraft departure noise source distribution (adapted from [39]).

The invention of the concept of high bypass ratio (HBR) turbofan engines , which was invented in the 1960s and which started getting implemented into commercial aircraft in the early 1970s, was a major breakthrough regarding engine jet noise reduction. The past efforts and achievements in the reduction of aircraft jet noise are visualised below in Figure 1.2, where various representative aircraft are chosen over the years and their effective perceived noise levels are illustrated. A clear reduction can be seen especially with the upcoming of the era of HBR engines.

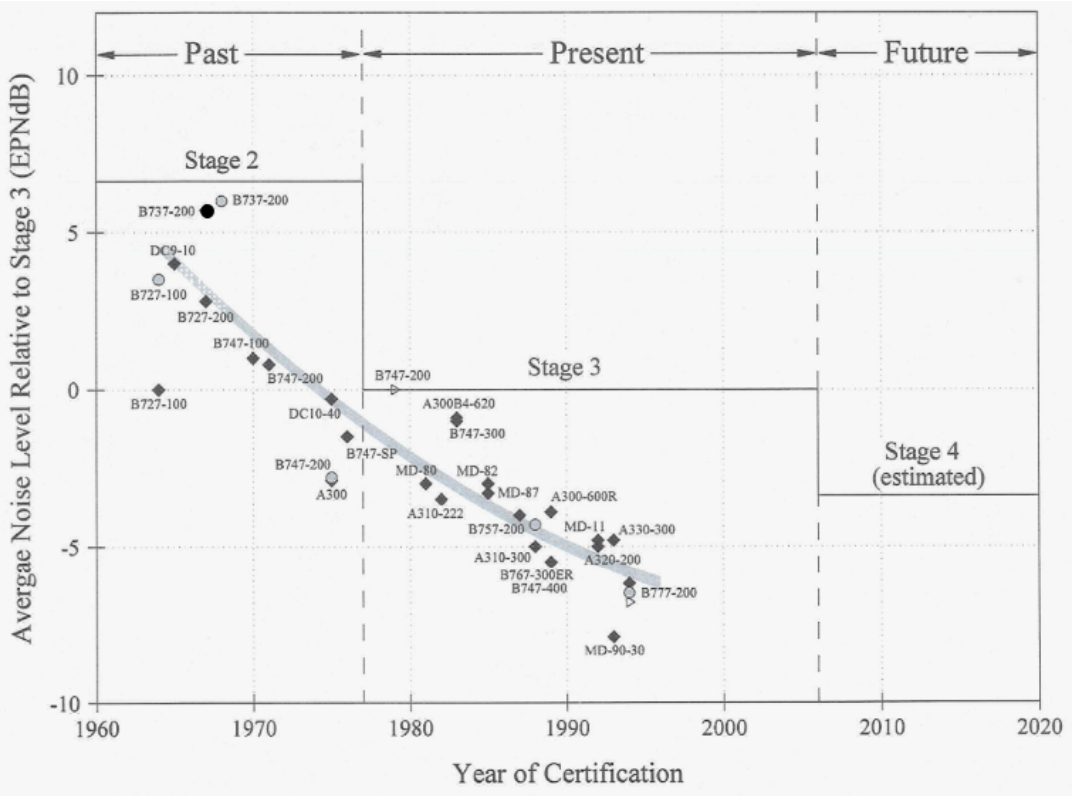

Figure 1.2: Effective Perceived Noise Levels of various representative aircraft over the years (taken from [26]).

With those clear advancements in noise reduction in the past, it is becoming progressively harder to maintain the trend in reduction in the recent years.
To summarize, the main breakthroughs in noise reduction concerning the aircraft jet engines follow the timeline given below:

- **Late 1950s**: Introduction of commercial jet aircraft, bringing significant noise challenges due to high-speed turbojet engines.

- **1960s**: Initiatives to modify airport operations and preliminary adjustments in engine designs to mitigate noise.
- **Early 1970s**: Introduction of high bypass ratio (HBR) turbofan engines, significantly quieter than turbojets.
- **1980s**: Use of advanced composite materials for fan blades and engine components.
- **Late 1980s**: Introduction of chevrons on engine nacelles and jet nozzles to reduce noise by smoothing exhaust gas mixing.
- **Early 2000s**: Emergence of active noise control technologies.
- **Mid-2000s**: Innovations like swept fan blades to reduce noise from blade tip vortices.
- **2010s**: Implementation of stricter ICAO Chapter 14 noise standards.
- **Ongoing**: Acoustic lining, Ultra-high bypass ratio engines, chevron nozzle refinement, active or closed-loop control, etc.

With these advancements in mind, the current thesis places itself in the broad category of jet noise reduction using active flow control which includes real-time adjustment and control of flow dynamics around aircraft surfaces, in this case the jet nozzle to be exact.

1.2. Research Objective & Questions

Given the information presented in the context of the literature study, an area of interest in research was obtained. This led to the following research question for this thesis:

How can synthetic jet actuators be designed to act on a subsonic jet for the purpose of jet noise mitigation?

To break down the aforementioned governing research question, the following research questions were posed:

1. What hydrodynamic structures within the jet should be actuated on to reduce overall noise?
   (a) What are the frequencies and the energy contents of structures within the jet that are responsible for the peak in the noise intensity spectra 72 nozzle diameters in the far field 90 degrees from the jet nozzle?
   (b) How can one predict the frequency and energy content numerically using experimental far-field noise spectra of the jet?
2. How can one design actuators that deliver sinusoidal fluctuations with energy content and frequency as outputted from 1(a)?
   (a) How effective are the piezoelectric-driven synthetic jet actuators in injecting the required energy into the flow at the desired frequency range?
   (b) What is the frequency response (velocity vs frequency) of the constructed actuator measured by a hot-wire?

As seen by the research questions, the project is therefore divided into two main parts comprising the theoretical identification of noise-producing structures in jets and the practical construction of actuators able to deliver the required outputs.

These research questions aim to guide the research in a structured manner and will henceforth be used as a guideline for the rest of the thesis.

1.3. Report Structure

This thesis is organized into six main chapters, each addressing a specific aspect of the research on turbulent jet aeroacoustic modeling and active flow control using synthetic jet actuators. The document begins with chapter 2 which delves into the fundamentals of jet flows and noise, exploring the aerodynamic principles behind jet turbulence, instabilities, and the mechanisms of noise generation, including an in-depth discussion on aeroacoustics and Lighthill's Acoustic Analogy. In chapter 3, the focus shifts to the development of a predictive model for jet noise, where the theoretical relationships between turbulence characteristics and far-field noise are examined. This chapter discusses the procedures used for fitting and optimization as well as the simplifications made in the mathematical model, culminating in a demonstration and evaluation of the model's effectiveness. The chapter 4 then takes all that information and proceeds to explore active flow control strategies, emphasizing the role of synthetic jet actuators in mitigating noise. It covers the various types of actuators, criteria for selection, and the working principles of synthetic jets, with a particular focus on piezoelectric-driven devices. Building on this, chapter 5 is dedicated to the design and theoretical modeling of piezoelectric-driven synthetic jet actuators, addressing the dynamics of the geometries that govern the actuator's performance. This chapter also considers the design aspects necessary to achieve specific energy and frequency objectives, model tuning, and the results from the actuator manufacturing and testing setup. The thesis concludes with chapter 6, which summarizes the key findings of the research, draws conclusions based on the outcomes, and offers recommendations for future research and potential developments in the field of jet aeroacoustics and active flow control technologies.

2

Turbulent Jet Flows & Noise

In this chapter, the fundamental definitions and descriptions of those flows are addressed followed by a more comprehensive description of their aerodynamics and acoustics. It aims to provide the basic theory behind jet flows which will put the reader into context and perspective, preparing them for the more intricate dynamics dealing with the aeroacoustic mechanisms of jet noise creation.

2.1. Fundamentals of Jet Flows

There exist various types of canonical jet flows, currently being studied based on the different conditions and configurations they pose. The most relevant to this thesis are the free jets which are characterized by a high-speed fluid discharging into a theoretically free medium without physical constraints. The jet freely mixes with the ambient environment which can be stationary or moving with a different velocity.

Throughout the entire duration of this thesis and therefore throughout the length of this report the term ”jet” will be referring to a round, axisymmetric (symmetrical properties around jet central axis), free, subsonic jet that is shooting directly in ambient, stagnant air.

2.1.1. Jet Structure

After precisely defining the geometry and explaining the assumptions of the jet to be studied, one can move on with the main defining variables of the jet. A simple free jet can be defined by two main parameters: the *nozzle exit diameter* D_j or simply d and the *jet exit velocity* U_j or U_0. Note that many quantities like the jet downstream position and the turbulence are expressed as a function of the nozzle exit diameter and the jet exit velocity respectively. One would for instance communicate that the fully-developed region of the turbulence in the jet is seen at about *8 diameters downstream* and that the turbulent structures fluctuate at around *10% of the jet exit velocity*.

Figure 2.1 and Figure 2.2 help understand the simple geometry of a round, axisymetric jet.

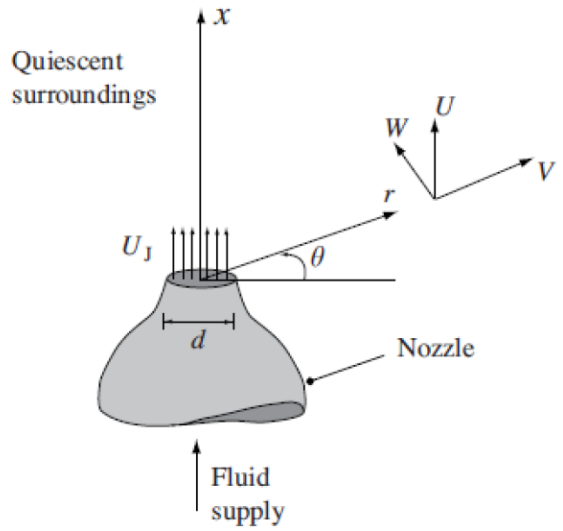

Figure 2.1: Geometry of a round, axisymmetric jet (sketch obtained from [9]).

In all discussions, the axis of symmetry will be referred to as the *jet centerline* and will be noted as the x-axis in illustrations. The main coordinate system used throughout the analyses is the one seen in Figure 2.2, with the jet centerline (x-axis) having its root in the middle of the circular nozzle exit section and pointing axially downstream. The y-axis corresponds to the radial direction (in the azimuthal plane). The angle that describes the offset from the jet centerline is referred to as the *azimuthal angle* and is shown as θ in Figure 2.2. This angle is particularly important since it is often used to describe concepts like the expansion of the shear layer or the directivity of the acoustic waves of the jet.

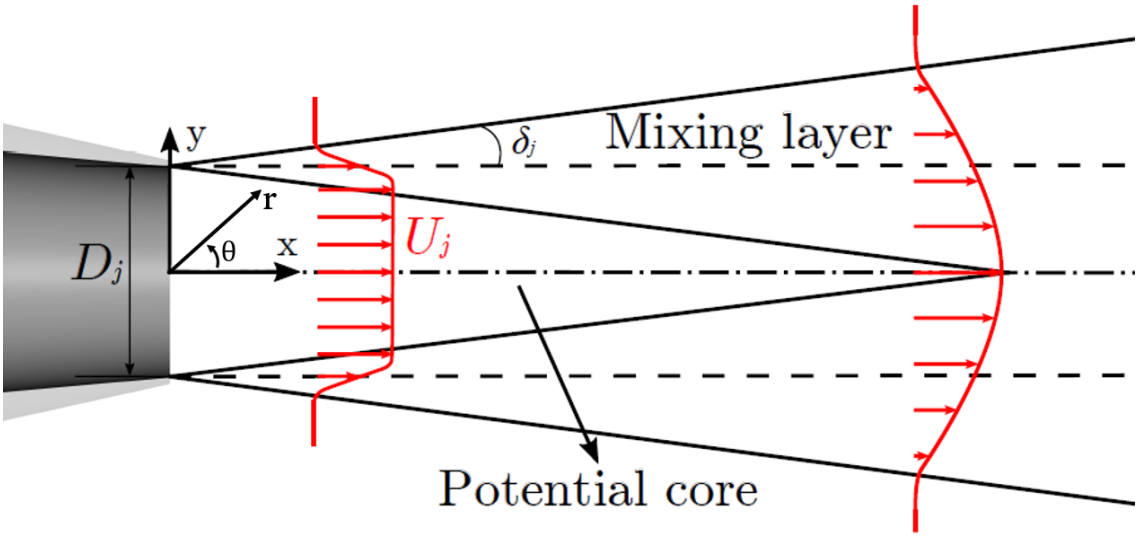

Figure 2.2: Main flow regions of a free jet and two velocity profiles highlighting the expansion of the jet wake (sketch adapted from [28]).

Figure 2.2 provides a visual representation of the main flow regions encountering with the jet creation. Below these are explained:

- **Potential Core**: This is the central region of the jet where the flow remains largely undisturbed and retains the maximum exit velocity of the nozzle. The potential core is a region of relatively

stable flow where the velocity does not decay, and the fluid properties are similar to those at the nozzle exit.

- **Shear/Mixing Layer**: Surrounding the potential core, the shear or mixing layer is where the high-speed jet fluid interacts with the ambient fluid. This layer is characterized by a high gradient in velocity between the jet stream and the surrounding medium. This region is found to be the most relevant for sound generation since the large velocity gradient causes instabilities which, as will be explained later, can amplify noise producing vortices.
- **Developed Turbulence**: Farther downstream from the nozzle exit, the flow loses its initial momentum, spreads laterally and transitions into fully developed turbulence while mixing with the ambient air. The sound generated here is found to be broad-spectrum since is a composite of noises produced by smaller-scale turbulent eddies.

The aforementioned structure of flow regions can be visualised in a very detailed LES of a Mach 0.9 jet performed by Bres et al. [1] as seen in Figure 2.3. The figure perfectly illustrates the existence of the shear layer which shows high temperature fluctuations due to the high turbulence associated with it, as well as the existence of the conical potential core bounded by the expanding shear layer after the jet nozzle exit.

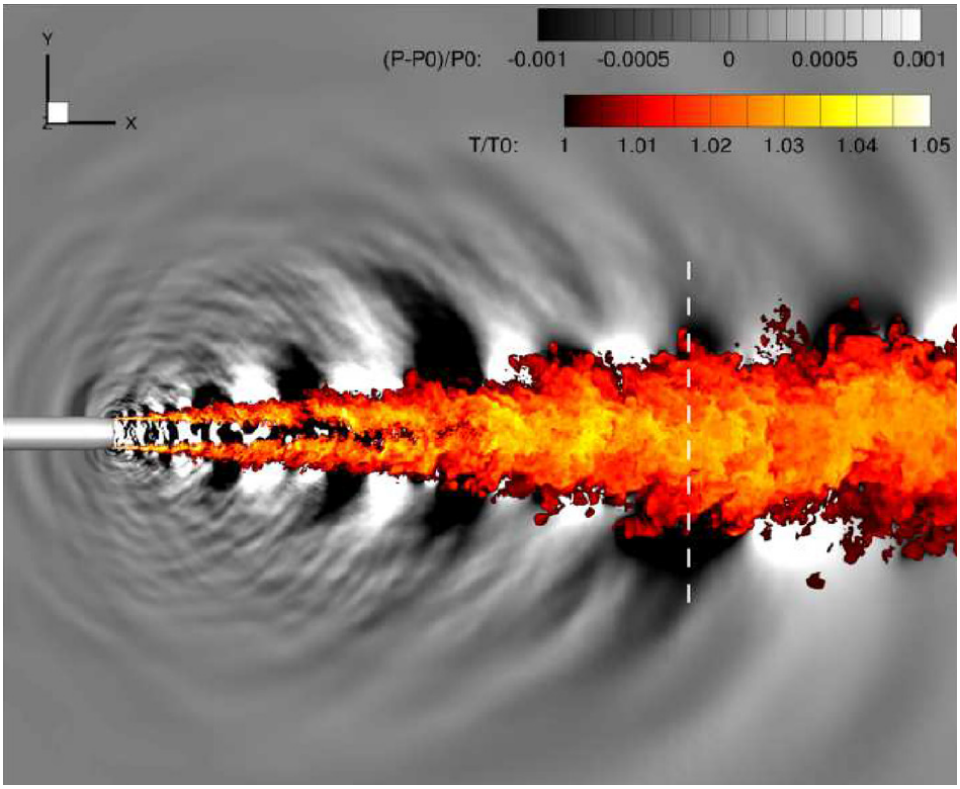

Figure 2.3: Temperature and pressure fluctuations of a Mach 0.9 jet (image obtained from the LES of Bres et al. [1]).

The figure also illustrates the fully turbulent flow region farther downstream at the wake of the jet as well as the acoustic emissions of the jet in terms of pressure fluctuations. The later will be the topic of discussion in the following sections and chapters.

2.1.2. Typical flow profiles and Self-similarity of Jets

An important property of the canonical subsonic jet flows is the one of *self-similarity*. Self-similarity means that profiles at various points in the jet can be collapsed into a single curve when normalized by local maximum values and characteristic dimensions, such as the jet width or velocity at the jet's centerline. Mathematically, the typical jet has been described by Equation 2.1 as seen below.

$$U = \begin{cases} U_{max} \exp\left[-\frac{(y \pm w_{core}/2)^2}{(w_{shear}/2)^2}\right] & \text{if } |y| > w_{core}/2 \\ U_{max} & \text{if } |y| \leq w_{core}/2, \end{cases} \tag{2.1}$$

Here one can see that for a given axial position, the velocity profiles are governed by a single formula which takes into account the local maximum velocity U_{max} located at the centerline as well as some measures of the width of the potential core w_{core} and the (half) width of the shear layer w_{shear} at that axial location.

Figure 2.4 provides a visual comparison of the theoretically calculated velocity profiles with experimental data for various axial locations. The self-similarity governing the jet is clearly observed.

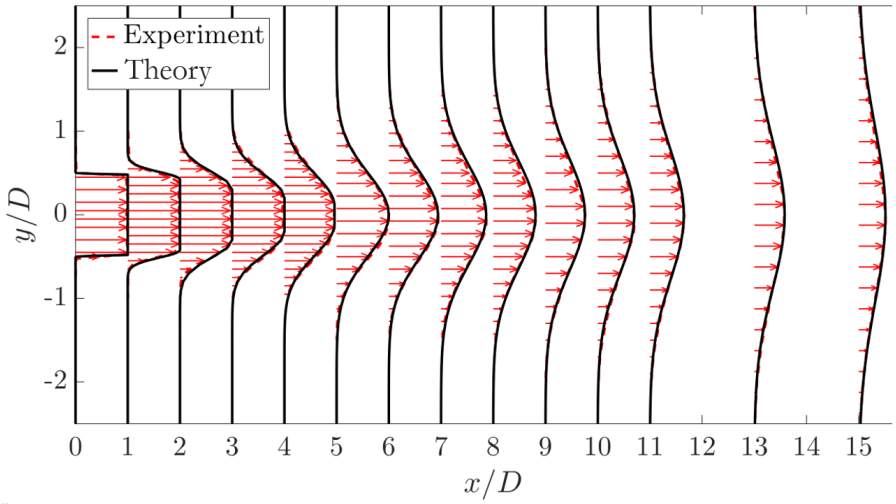

Figure 2.4: Theoretical and experimental velocity profiles downstream of the jet exit (image adapted from [45]).

This concept of self-similarity streamlines the complexity of jet flow analysis and is foundational in theoretical models that predict jet behavior and noise. More specifically, as it will be relevant in the next chapter, self-similarity in aeroacoustics helps in modeling how noise generated by jets disperses and decays. Just like velocity, the noise spectra also exhibit self-similarity in a similar fashion [51].

2.2. Jet Aerodynamics

Understanding jet flow aerodynamics is crucial for advancing aeroacoustics and noise reduction applications. The dynamics of jet flows directly influence the generation and propagation of sound waves, with aspects like turbulence intensity playing key roles in the acoustic signature of jets. By analyzing these aerodynamic properties, one can develop more effective strategies to reduce noise which is the scope of this thesis project. The last discussion regarding aerodynamic instabilities is particularly important since they are believed to be the main source of noise and scientists are focused on suppressing them [14].

2.2.1. Turbulence in jets

Since the first attempts to study jet flows in the context of aeroacoustics by Lighthill, it was understood that the key to explaining sound was to identify sources of noise within the flow, therefore requiring a clear understanding of the underlying turbulence [20]. It was also observed very early how only a very small percentage of the total jet power through turbulent kinetic energy within the flow would manage to escape the jet as acoustic energy [18]. This interaction of the two separate fields observed in a jet flow, namely the high-energy, chaotic, turbulent field resulting in a low-energy acoustic one, is of main interest in this section.

A canonical jet flow, while complex, has been categorized into several distinct regimes, each characterized by different physical phenomena and mathematical descriptions. These regimes can be identified based on the order of the pressure fluctuations within the flow as seen in Figure 2.5 [49].

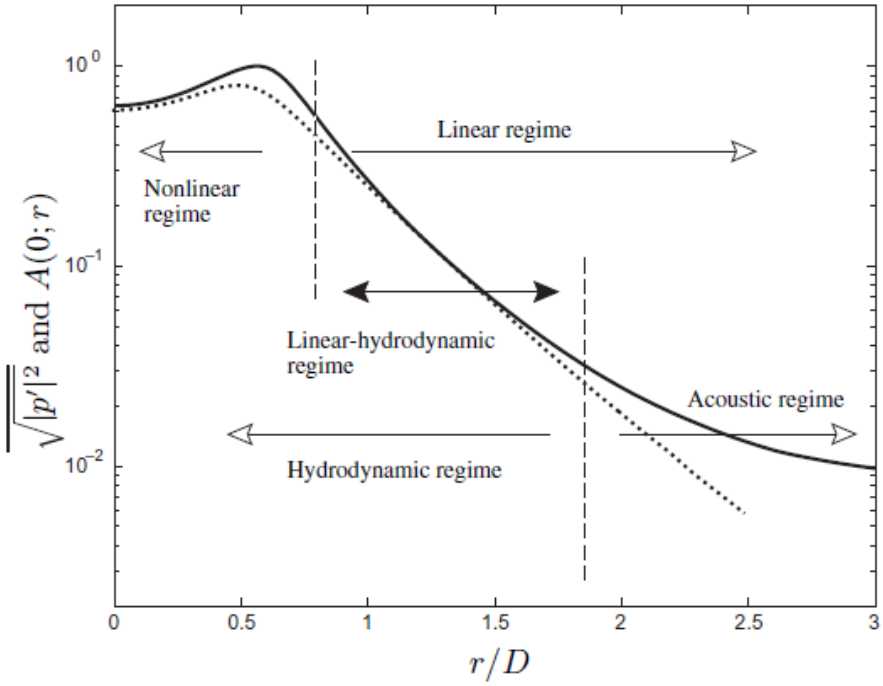

Figure 2.5: Pressure fluctuations dictating different flow regimes in the radial direction (obtained from [49]).

This figure highlights two important distinctions based on the order of the pressure fluctuations and in which radial position they are found.

Firstly, there is the linear region of turbulence, characterized by smaller pressure fluctuations. The interactions between different turbulent scales are minimal, leading to more straightforward mathematical modeling. On the other hand, structures occupying the highest part of the pressure fluctuation constitute the non-linear regime. This region is dominated by large fluctuations and the complex interactions between scales of motion make linear theories fail to predict. The unpredictability and complexity of the non-linear regime of the flow make it challenging to predict and require advanced simulation techniques like LES or DNS.

The second distinction that is made in Figure 2.5 is the one between the hydrodynamic and the acoustic regime of the flow since they represent fundamentally different aspects of fluid behavior. The hydrodynamic region is dominated by inertial forces, focusing on momentum and mass transfer through turbulent mixing, which are essential for the shaping and spreading of the jet. In contrast, the acoustic region is characterized by the dominance of sound waves, where the main concerns are the propagation of these waves with minimal influence from turbulence, analyzed through the linearized equations of acoustics. Obviously, the acoustic regime concerns pressure fluctuations with a very low order while the hydrodynamic region contains a large range of scales that also interact with each other in the non-linear regime.

Given the previous distinctions, the scientific community has decided to split the turbulence encountered in jet flows into two main categories [24] [46] [53]:

- **Fine-scale turbulence:** This refers to smaller, more random turbulent structures within the jet flow. The noise produced by fine-scale turbulence typically manifests at higher polar angles and is characterized by lower correlation levels in the far-field measurements. This type of turbulence does not have coherent structures and contributes to the fine-scale similarity shape of the noise

spectrum as discussed earlier.

- **Large-scale turbulence:** These are larger, more coherent turbulent structures in the jet flow. They are significant noise contributors, particularly at lower polar angles and in the aft radiation directions (directivity). The noise from these structures is highly correlated at specific angles and conforms to the large-scale similarity shape in the noise spectrum. The large-scale structures can play a crucial role in noise generation even at lower jet velocities.

This distinction is still relevant as shown in recent work on jet noise-source modelling like the one by Bychkov et al. where jet noise is modelled using two approaches derived from the different behaviour of the small vs the large turbulent scales [41].

As hinted previously, the turbulence has some intrinsic self-similarity just like the velocity profiles [47]. Turbulence is usually characterized by its intensity because, due to its chaotic nature, is usually modelled in a stochastic form. The turbulence intensity (TI) is the statistical parameter defined as the statistical mean (RMS) magnitude of the velocity fluctuations at a specific location normalised by the actual magnitude of the velocity at the given location.

$$TI = \frac{u'}{U} \tag{2.2}$$

with the velocity fluctuations calculated as follows:

$$u' = \sqrt{\frac{1}{N}\sum_{i=1}^{N}(u_i - \overline{u})^2} \tag{2.3}$$

The last equation represents the calculation of the mean fluctuations of the localized flow velocity based on the RMS of multiple instances (u_i) of the actual flow velocity minus the time averaged one ($\overline{u}$). The TI is effectively a measure of the magnitude of the velocity fluctuations as a percentage of the overall velocity. The self-similarity of the turbulence can be quantitatively observed in the profiles of turbulence intensity of the jet. This is visible in Figure 2.6 where multiple profiles of the TI are shown for the different jet downstream positions.

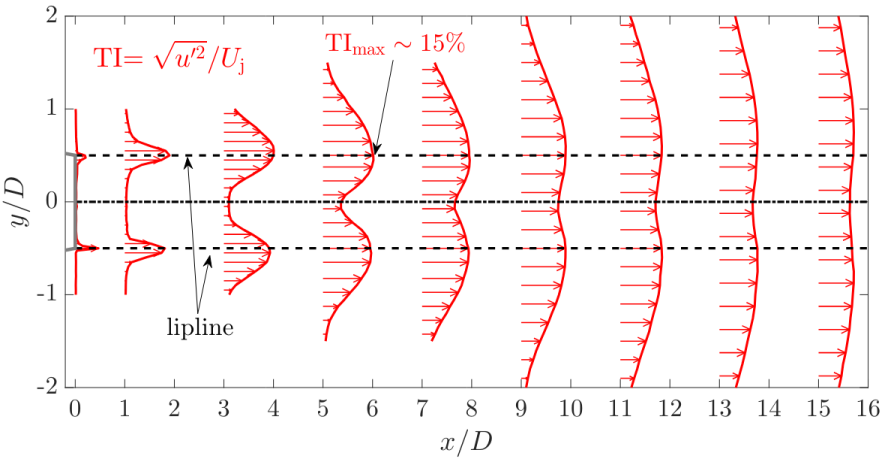

Figure 2.6: Experimental turbulence intensity for a Mach 0.6 jet (image obtained from [45]).

For the context of aeroacoustics, turbulence intensity is an important statistical parameter that directly relates to sound generation. Since jet flows are turbulent flows, high turbulence implies large velocity fluctuations which correspond to high kinetic energy which in turn can correspond to higher acoustic emissions.

It is therefore evident how proper turbulence modelling is a crucial step for jet sound generation prediction through noise modelling. The most relevant instance of noise modelling which takes into account turbulence modelling is the noise model by Morris and Farassat ([21]) which builds upon the basic sound generation model also known as Lighthill's acoustic analogy ([19]). The aforementioned model by Morris and Farassat bases its sound generation function on the appropriate characteristic scales of the flow turbulence. To obtain those turbulent scales they use the statistical properties following the solution of the Reynold's-averaged Navier-Stokes equation which in turn utilizes a k-ϵ turbulence model [21].

This sound generation model, as will be seen later, will form the theoretical basis of a conceptual jet sound-source characterization model developed with the aim to locate and characterize the scales of the turbulent structures within a jet which are expected to be the most noise-producing given an experimental sound spectrum. One of the model's biggest assumptions corresponds to that of characterizing turbulence.

2.2.2. Instabilities

Earlier, a distinction was made regarding the size and scale of the turbulence. One of the two distinct characterizations of turbulence was that where large, more coherent structures can be spotted. These structures are usually a product of flow instabilities within the jet which tend to amplify specific structures and cause this distinct coherence [49]. These instabilities are primarily associated with the shear layers in the jet, where the high-speed jet fluid interacts with the surrounding stationary air.

The most relevant instability in jets is the Kelvin Helmholtz instability. This is the primary instability mechanism observed in jet shear layers. It arises due to the velocity gradient at the interface between the fast-moving jet and the slower-moving ambient air. The differential in velocity across the shear layer makes the flow susceptible to perturbations, which can grow exponentially, manifesting as wave-like structures along the shear layer. These structures are often modeled as rolling up into vortices, which eventually break down into smaller turbulent structures further downstream. Unavoidably, due to the 3D nature of the jet, beyond the initial instabilities driven by the Kelvin-Helmholtz mechanism, streamwise or longitudinal vortices can form due to the complex three-dimensional strain rates within the turbulent jet. [52]

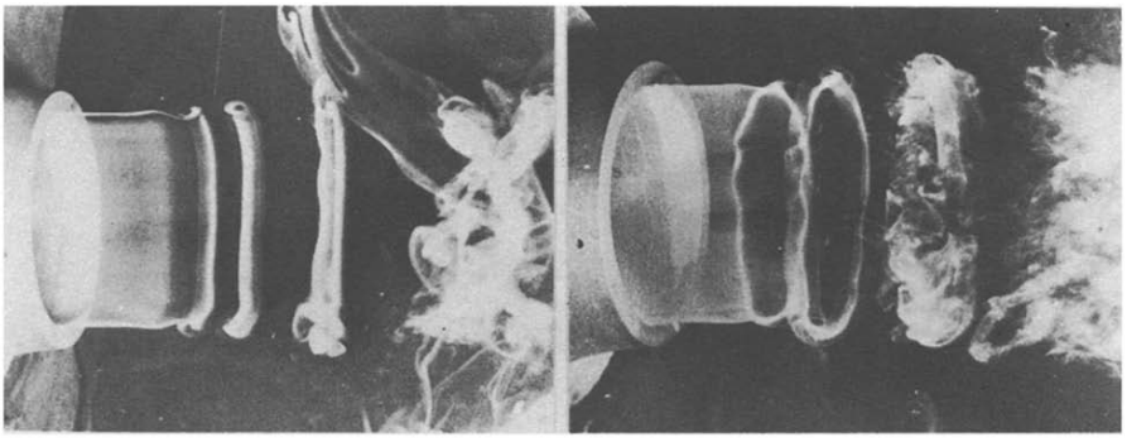

Figure 2.7: Visualization of subsonic jet instabilities in the shear layer (image obtained from [6]).

In Figure 2.7 one can see the instability initiating from the jet nozzle and its "divergence" as it travels through the shear layer. As always far enough downstream it breaks down into the standard chaotic turbulence.

Since these structures show some ordering in space in time, they are blamed by many as the most noise

inducing turbulence mechanism. For that reason numerous researches are focusing on acoustically exciting the jets in order to break down these instabilities and suppress their noise-creating nature (see one of the most recent efforts to control instability waves by Kopiev et al. [14]).

2.3. Jet Noise Mechanisms

This section first explores the basic principles of aeroacoustics in jets through the various aeroacoustic analogies with Lighthill's analogy as the basis. Later, the role of coherent structures in noise generation will be highlighted and connected to the general concept of flow instabilities found in jet flows as described in the previous chapter. These coherent structures are considered to be essential features in the acoustic signature of jet flows [15] [43].

2.3.1. Aeroacoustics of Jets

The theoretical framework for sound generation in aeroacoustics often relies on analogies with classical acoustics. Since only a tiny fraction of the turbulent flow energy is converted into sound, careful modeling needs to take place in order to accurately analyse the aeroacoustics of a jet [18]. Rienstra's comprehensive book on acoustics provides a summary of the foundations that underpin the more specialized field of aeroacoustics [48]. Hirschberg's introduction on aeroacoustics also presents these analogies in detail, starting from basic acoustic principles and extending to the complexities of aeroacoustic phenomena [4].

Several theoretical models have been proposed to predict jet noise, including those by Lighthill and subsequent modifications and improvements. Lighthill's acoustic analogy laid the foundation for understanding jet noise by approximating the sound field as a perturbation of an idealized reference flow [19]. It represents the Navier-Stokes equations but expressed in a wave-like form such that it can describe the sound propagation. This model identifies differences between the actual turbulent jet flow and the reference flow as sources of sound [19]. Its importance in aeroacoustics is so crucial so a specific section is later devoted just for this analogy. The paper by Ahuja and Bushell effectively uses classical acoustic analogies, primarily Lighthill's theory, to interpret and validate experimental data on subsonic jet noise. While the experimental results generally support Lighthill's predictions, they also reveal areas where the theory does not fully align with observed phenomena, particularly in high-frequency ranges and near the jet axis [22].

Additionally, Tam's review on turbulence mixing noise mechanisms since 1952 offers a historical perspective on the development and refinement of these models [51]. In the review it is emphasized how the jet noise comprises two main components: noise from large turbulence structures/instability waves and noise from fine-scale turbulence, applicable to both subsonic and supersonic jets. More relevant to subsonic jets, fine-scale turbulence predominates except in specific directions (remember the directivity to the inherent jet instabilities). Moreover Tam highlights that noise intensity is influenced mostly by jet velocity as well as temperature and radiation direction, with empirical scaling laws aiding prediction and extensive experimental data validating these theoretical predictions. Tam's contributions emphasize the role of turbulence in noise generation and the evolution of predictive models over time, always starting with Lighthill's analogy as the basis.

Understanding the sources of subsonic jet noise has been greatly advanced by diagnostic studies that focus on measurement techniques for source identification. Suzuki's review highlights various approaches and technologies used to diagnose jet noise sources and provides a comprehensive understanding of the subsonic noise generation mechanisms [49]. These diagnostic methods are crucial for identifying the specific areas within the jet flow that contribute most significantly to noise production.

Moreover, advancements in computational fluid dynamics have enabled more accurate simulations of jet turbulence and noise. For instance, Bres et al.'s simulations of the nozzle exit boundary layer have achieved predictions of noise levels within 0.5 dB of experimental measurements, showcasing

the progress in predictive modeling capabilities [1]. These simulations provide a detailed view of the flow structures and their noise-generating mechanisms, facilitating better noise control strategies.

Finally, in the context of jet noise control, the book by Ginevsky et al. provides an extensive overview of acoustic control methods for turbulent jets, highlighting different techniques and their effectiveness in noise reduction [46]. Acoustic control methods, such as altering the jet's structure through the jet's natural instabilities, are essential for mitigating the adverse effects of jet noise as will be seen in the 2nd part of the thesis development.

2.3.2. Lighthill's Acoustic Analogy

In turbulent jets, such as those found in unsteady flows, minor pressure variations are created within the flow. These fluctuations travel outward at the speed of sound and continue over extended distances, forming what is recognized as the acoustic field. In this field, the behavior of these sound waves adheres to the homogeneous wave equation, a scenario often referred to in general as aerodynamic sound. [11]

Lighthill's acoustic analogy provides a theoretical framework for analyzing the generation of sound by turbulent fluid flows. **The theory of this section is taken directly from the first work of Lighthill regarding the jet noise and is highlighted as its solution will form the basis of the predictive model developed later [19].** This analogy rearranges the equations of fluid dynamics into a form that is suitable for acoustic analysis. The starting point is the compressible Navier-Stokes equations.

Basic Formulation

The basic idea of Lighthill's analogy is to rewrite the conservation equations for mass and momentum to form an inhomogeneous wave equation. The continuity equation for a compressible fluid is given by Equation 2.4:

$$\frac{\partial \rho}{\partial t} + \nabla \cdot (\rho \mathbf{u}) = 0, \tag{2.4}$$

where ρ is the fluid density and $\mathbf{u}$ is the velocity vector.

The momentum equation is given as in Equation 2.5:

$$\frac{\partial (\rho \mathbf{u})}{\partial t} + \nabla \cdot (\rho \mathbf{u}\mathbf{u}) = -\nabla p + \nabla \cdot \tau + \mathbf{f}, \tag{2.5}$$

where p is the pressure, τ is the viscous stress tensor, and $\mathbf{f}$ represents external forces per unit volume.

Lighthill's Wave Equation

Lighthill's acoustic analogy reformulates these equations to derive a wave equation for the fluctuating part of the density, $\rho' = \rho - \rho_0$, where ρ_0 is the mean density. By manipulating the continuity and momentum equations, Lighthill obtained the following wave equation for ρ' as shown in Equation 2.6:

$$\frac{\partial^2 \rho'}{\partial t^2} - c_0^2 \nabla^2 \rho' = \nabla \cdot \nabla \cdot \mathbf{T}, \tag{2.6}$$

where c_0 is the speed of sound in the medium and $\mathbf{T}$ is the Lighthill stress tensor given by Equation 2.7:

$$T_{ij} = \rho u_i u_j + \left(p - c_0^2 \rho\right) \delta_{ij} - \tau_{ij}. \tag{2.7}$$

Source Terms

The term $\nabla \cdot \nabla \cdot \mathbf{T}$ represents the source of sound generated by turbulence and other flow phenomena. The Lighthill stress tensor $\mathbf{T}$ encapsulates the contributions from the Reynolds stresses, pressure fluctuations, and viscous stresses as expanded in Equation 2.8:

$$\nabla \cdot \nabla \cdot \mathbf{T} = \frac{\partial^2}{\partial x_i \partial x_j} \left(\rho u_i u_j + \left(p - c_0^2 \rho\right) \delta_{ij} - \tau_{ij}\right). \tag{2.8}$$

Implications

Lighthill's analogy is particularly powerful because it allows for the treatment of sound generation as a problem in linear acoustics, with the source terms providing the necessary link to the complex, non-linear dynamics of the turbulent flow. This framework is widely used in aeroacoustics to predict and analyze the sound generated by various flow configurations, such as the jet noise and sound from turbulent boundary layers and is used in the next chapter to link the hydrodynamic field of jets to the far field noise.

In summary, Lighthill's acoustic analogy transforms the problem of aerodynamic sound generation into a form that can be more easily analyzed using the tools of linear acoustics, providing the link between fluid dynamics and acoustics. The solution of Lighthill's analogy is used in the next chapter as the basis of the theoretical noise-source prediction model as developed by Morris and Farassat [21].

2.3.3. Coherent Structures in Noise Generation

Previously, the concept of instabilities inside the jet was introduced and briefly explained. In the context of noise generation there is one type of coherent structures which has grabbed the interest of researchers and which has been given the special name of wave packets. The review by Jordan and Colonius provides a good summary of the noise generation mechanisms of those wave packets [43].

Wave packets are structures spatiotemporally coherent over large distances relative to the integral scales of turbulence in the jet. Despite their relatively low energy compared to the overall turbulent field, their high space-time coherence makes them significant for noise generation and this is therefore the reason why multiple research focuses on understanding those structures.

These structures have been studied starting with basic linear stability theories to developing very complex prediction models that involve non-linear dynamics. An instance of models developed for wave packets are presented by Cavalieri et al. and touch upon Lighthill's acoustic analogy as well as the linearized version of the homogeneous Navier-Stokes equations [15]. A lot of attention is nowadays given to proper orthogonal decomposition of the flow and analysis of the acoustic modes [12] [7]. All these purely mathematical analyses are a tool to identify coherence in the flow like the one observed with wave packets. At the same time, really involved models are being developed incorporating non-linear dynamics like the one by Zhang et al. which presents a recent model for sound generation in jets that delves deep into the modal structures using non-linear dynamics [55].

The existence of those structures through the instabilities in the shear layer causes a directivity in the sound generation observed at an angle of about 20-30 degrees downstream [41]. This directivity can be observed in the noise spectra in the farfield at these small downstream angles [23].

Despite the efforts for understanding the identification and behaviour of those coherent structures as noise sources, the mechanisms of noise creation are still not clear. The problem of the complexity of those structures within the highly turbulent context of the jet has been tried to be solved by pure simulations like the one by Freund [8]. Regardless, in the context of this thesis a more general approach will be taken with regards to noise source identification which does not require the mathematical complexity of the developed noise source models through modal analysis nor the computational power of simulating fields.

3

Jet Noise-Source Prediction Model

This chapter will present the theory, development and results of the noise-source prediction model developed throughout this thesis in order to define a ”range of interest” regarding the frequency and energy of the most noise-inducing structures in the jet. Firstly, the fundamental theory of the predictive model will be introduced based on the corresponding acoustic analogy as described in the previous chapter. This theory will provide a mathematical framework linking turbulence characteristics to far-field noise. Afterwards, the mathematical simplifications of the model will be analysed and the steps on making it into an optimization problem will be highlighted. The chapter will conclude by addressing the results obtained from the developed model and discussing the limitations inherent in the current modeling approach.

3.1. Relation of turbulence characteristics to far-field noise

This section presents the theoretical basis that is used by the predictive model in the following sections. It is based on the methodology by Morris and Farassat and it is a solution of Lighthill's acoustic analogy that is enriched by turbulent statistics models to provide solutions for the noise intensity spectrum at the far field of a jet [21]. Note that since the early days of jet aeroacoustics, the main theory of Lighthill was used to predict the noise spectrum and was then compared to experimental data [22].

Since the model utilizes turbulence data, the first step is performing a RANS with will give the $k-\epsilon$ solution together with the characteristics scales of the flow. The noise contributions of those scales are the calculated from the derived spectrum intensity formula and are then summed up. The end result is the complete spectrum of intensity density which can then be compared to experimental data.

This section explains the process behind this calculation and in the later sections the process of how this methodology is used to achieve the backwards result will be explained. **Note that the theory of the following section is taken directly from Morris and Farassat with the purpose to be used later on by the predictive model [21].**

3.1.1. Solution of Lighthill's acoustic analogy

The solution for the far field density fluctuations at a time t following Lighthill's basic acoustic analogy is given by Equation 3.1. Note that the Lighthill stress tensor is simplified to $T_{ij} = \rho_s u_i' u_j'$, under the assumption that viscous terms are ignored and that since the analysis is done for $\theta = 90^o$ to the jet axis, the majority of the contributions to the tensor are products of the velocity fluctuations (pure turbulence).

$$\rho'(\boldsymbol{x},t) = \frac{1}{4\pi c_0^4}\frac{1}{x}\iiint_{V(\boldsymbol{y})}\frac{\partial^2}{\partial t^2}T_{xx}\left(\boldsymbol{y}, t-\frac{|\boldsymbol{x}-\boldsymbol{y}|}{c_0}\right)\mathrm{d}\boldsymbol{y} \tag{3.1}$$

In this current report for the sake of compactness, the time of ”emission” by the source will be defined as:

$$t_{emit} = \frac{|\boldsymbol{x} - \boldsymbol{y}|}{c_0} \tag{3.2}$$

where $|\boldsymbol{x} - \boldsymbol{y}|$ represents the distance between the far field observer $\boldsymbol{x}$ and the source $\boldsymbol{y}$. After dividing by the speed of sound this expression gives the time required for an acoustic emission from the source to reach the location of the observer in the far field.

Equation 3.1 then describes the density fluctuation at time t resultant from the turbulent characteristics given by the stress tensor T_{xx} of the source at time $t - t_{source}$.

3.1.2. Relation to far field spectral intensity function

The formula stating the relation of the far-field intensity density in the spectral domain is given by Equation 3.3 below.

$$S(\boldsymbol{x}, \omega) = \frac{1}{2\pi} \int_{-\infty}^{\infty} \frac{\langle p'(\boldsymbol{x}, t) p'(\boldsymbol{x}, t + \tau) \rangle}{\rho_0 c_0} e^{i\omega\tau} \mathrm{d}\tau \tag{3.3}$$

which contains the autocorrelation function taken at the pressure on the far field. This parameter represents the sound intensity divided per the frequency brackets across the spectrum. Attention should be given at the unit of this spectrum which is $W/m^2/Hz$ and where the normalization of the sound intensity (W/m^2) is divided by the frequency brackets (Hz) resulting in the intensity density across the frequency spectrum.

Given the model is for far field operation, the simple Equation 3.4 relating the pressure and density wave fluctuations through the square of the speed of sound.

$$p' = c_0^2 \rho' \tag{3.4}$$

This relation can be substituted into Equation 3.3 resulting in Equation 3.5 which contains the turbulence information from the stress tensor of Lighthill in the source and gives the corresponding intensity density in the spectral domain.

$$S(\boldsymbol{x}, \omega) = \frac{1}{32\pi^3 \rho_0 c_0^5 x^2} \int_{-\infty}^{\infty} \int_{V(y_1)} \int_{V(y_2)} \left\langle \frac{\partial^2 T_{xx}}{\partial t^2} (\boldsymbol{y}_1, t_1) \times \frac{\partial^2 T_{xx}}{\partial t^2} (\boldsymbol{y}_2, t_2) \right\rangle e^{i\omega\tau} \mathrm{d}\boldsymbol{y}_1 \, \mathrm{d}\boldsymbol{y}_2 \, \mathrm{d}\tau \tag{3.5}$$

with $t_1 = t - t_{emit,1}$ and $t_2 = t - t_{emit,2} - \tau$ (refer to definition of t_{emit} above).

3.1.3. Two-point cross-correlation of turbulent field

Since it is assumed that the flow is statistically stationairy, stationairy turbulence statistics are assumed by extent. This means that in Equation 3.5 the 2nd derivatives of the stress tensors can be stacked and separated from the main expression, leaving the two-point cross-correlation isolated. Since this term is the one of importance, it is worth noting the distinct expression for its function. Equation 3.6 explicitly defines R_f as the two-point cross-correlation of Lighthill's stress tensor T_{xx} and will be used in the later steps to simplify the modelling.

$$R_f\left(\boldsymbol{y}_1, \boldsymbol{\eta}, \tau\right) = \left\langle T_{xx}\left(\boldsymbol{y}_1, t\right) T_{xx}\left(\boldsymbol{y}_2, t+\tau\right)\right\rangle \tag{3.6}$$

with $\eta = y_2 - y_1$.

With this two-point cross-correlation, the spectrum of frequency in combination with wave number α is calculated as in Equation 3.7. This formula is effectively describing the periodic nature of the sources spatially and temporally.

$$H\left(\boldsymbol{y}_1, \boldsymbol{\alpha}, \omega\right) = \frac{1}{(2\pi)^4} \int_{V(\xi)} \int_{-\infty}^{\infty} \exp[i(\omega\tau - \alpha \cdot \boldsymbol{\xi})] \quad \times R_m\left(\boldsymbol{y}_1, \boldsymbol{\xi}, \tau\right) \mathrm{d}\boldsymbol{\xi} \mathrm{d}\tau \tag{3.7}$$

Note that here the two-point cross-correlation function has been moved from a fixed (R_f) to a moving frame of reference (R_m) through $\xi = \eta - ic_0 M_c \tau$ with i being the unit vector of the mean flow and M_c the convection Mach of the turbulent vortices. This wave number/frequency formulation helps incorporate the turbulence statistics models into the cross-correlation function and will be the beginning of modelling freedom as it is the first point where assumptions other than the far field assumption will have to be introduced. Note again that this information and formulas are taken directly from the work of Morris and Farassat therefore for more details behind the mathematics refer to the original paper [21].

Incorporating the correlation formulation described in Equation 3.7 (through the definition of Equation 3.6 and after transferring it into a moving reference frame) into the big expression of the intensity density Equation 3.5 (given that the ensemble average of the stress tensors can be separated from the derivatives as explained above), results in Equation 3.8.

$$S(x, \omega) = \frac{\pi \omega^4}{2\rho_0 c_0^5 x^2} \int_{V(y_1)} H\left(y_1, \frac{\omega}{c_0}, \omega(1 - M_c \cos\theta)\right) dy_1 \tag{3.8}$$

with defined as $cos\theta = \frac{x_1}{1}$. This expression will be the basis of the model. By introducing different expressions for the wave number/frequency spectrum created by the sources of turbulence, one can expect to get different results when it comes to the intensity spectrum of noise in the far field.

3.1.4. Modelling for turbulent statistics

The next step is that of introducing a model for the two-point cross-correlation. The simple case assumes a Gaussian cross-correlation formulation which in the moving reference frame would look as in Equation 3.9, where A is a measure of the correlation.

$$R_m(y_1, \xi, \tau) = A^2 \rho_s^2 u_s^4 \exp\left(-\frac{|\xi|^2}{l_s^2} - \omega_s^2 \tau^2\right) \tag{3.9}$$

This correlation formula contains the following characteristic scales:

- ρ_s - characteristic scale of density
- u_s - characteristic scale of velocity fluctuations (in turbulence)
- ℓ_s - characteristic length scale
- ω_s - characteristic frequency scale

.

Substituting the two-point cross-correlation Gaussian formulation in the moving reference frame of Equation 3.9 into the expression for the source spectrum as in Equation 3.7, one gets Equation 3.10.

$$H\left\{\boldsymbol{y}_1, \frac{\omega \boldsymbol{x}}{x c_0}, \omega\left(1 - M_c \cos\theta\right)\right\} = \frac{A^2}{(2\pi)^4}\rho_s^2 u_s^4 \frac{\pi^2 \ell_s^3}{\omega_s} \times \exp\left\{-\frac{\omega^2\left(1 - M_c\cos\theta\right)^2}{4\omega_s^2}\right\} \exp\left\{-\frac{\left(\alpha \ell_s\right)^2}{4}\right\} \tag{3.10}$$

To summarize, Equation 3.10 describes the far field spectrum (in the frequency domain) of a turbulent source system which can be described based on characteristics scales of the flow as explained above.

At this point, an important assumption is made that simplifies Equation 3.10:

- The last term $\exp\left\{-\frac{\left(\alpha \ell_s\right)^2}{4}\right\}$ in the equation can be dropped since the term $\alpha \ell_s$ (wave number times characteristic length scale) effectively describes $\frac{u_s}{c_0}$ which is assumed very small since the turbulent velocity fluctuation scales u_s are obviously much smaller than the speed of sound. This term is thus close enough to unity and can therefore be neglected.

Note that the following analysis including the fitting to experimental data will be performed for the special case of the far field at $\theta = 90^o$ angle which is effectively the far field of the axisymmetric jet at the same plane as the nozzle exit. Even though this does not correspond to the angle of maximum noise emissions for jets (since the directivity effects of the instabilities do not have an effect at $\theta = 90^o$), it will provide the starting point for future analysis.

Following the previous statement, an extra simplification can be made to Equation 3.10:

- The term $\left(1 - M_c \cos\theta\right)^2$ in the equation can be dropped. Since $\theta = 90^o$, the cosine is zero so the whole term end up being unity and so it can be omitted from the equation.

With the aforementioned simplifications, Equation 3.10 takes the following form:

$$H\left\{\boldsymbol{y}_1, \frac{\omega \boldsymbol{x}}{x c_0}, \omega\right\} = \frac{A^2}{(2\pi)^4}\rho_s^2 u_s^4 \frac{\pi^2 \ell_s^3}{\omega_s} \times \exp\left\{-\frac{\omega^2}{4\omega_s^2}\right\} \tag{3.11}$$

This simplified version of the turbulence correlation of Equation 3.11 is then ready to be plugged into the intensity density formula of Equation 3.8, resulting in Equation 3.12 as taken from Morris and Farassat and that represents the contribution of each infinitesimal volume to the overall spectra given specific characteristic scales.

$$\mathrm{d}S(x,\omega) = \frac{A^2}{32\pi\rho_0 c_0^5 x^2}\left\{\rho_s^2 u_s^4 l_s^3 \omega_s^3 \left(\frac{\omega}{\omega_s}\right)^4 \exp\left(-\frac{\omega^2}{4\omega_s^2}\right)\right\}\mathrm{d}V \tag{3.12}$$

3.1.5. Introducing a turbulence model

For the turbulent scales a $k-\epsilon$ RANS model will be used [21]. This way, a reduction of the variables contained in Equation 3.12 can be achieved. The exact assumptions are stated below:

- $\omega_s = \frac{2\pi}{\tau_s}$
- $\tau_s = c_\tau\left(\frac{k}{\epsilon}\right)$
- $l_s = c_l\left(\frac{k^{\frac{3}{2}}}{\epsilon}\right)$

This formulation effectively utilizes two extra parameters k and ϵ, each with their own transport equations which are not relevant here. The first one, k, corresponds to the kinetic energy, which represents the energy contained in the turbulent eddies. This is the main parameter of interest since it can be used to understand the energy content of relevant structures which helps identify them and target them for the purpose of control. The physical formula for this parameter is given below in Equation 3.13 and it represents the sum of the mean square of the velocity fluctuations in all 3 degrees of freedom in the context of the fluctuating turbulent components of the velocity field that contribute to the energy.

$$k = \frac{1}{2}\left(\overline{u'^2} + \overline{v'^2} + \overline{w'^2}\right) \tag{3.13}$$

The second one, ϵ, represents the dissipation rate of the turbulent kinetic energy, which describes the rate at which the energy is dissipated within the turbulent flow.

This is how the relevant characteristic scales relate to the kinetic energy k and its dissipation rate ϵ:

- Turbulence characteristic length scale:
$$l_s \sim \frac{k^{3/2}}{\epsilon}$$
- Turbulence characteristic time scale:
$$\tau_s \sim \frac{k}{\epsilon}$$

Having defined these two characteristic scales above, the following characteristics scales will be used in the modelling as seen in Equation 3.14.

$$\omega_s = \frac{2\pi}{\tau_s}, \qquad \tau_s = c_\tau\left(\frac{k}{\epsilon}\right), \qquad l_s = c_l\left(\frac{k^{3/2}}{\epsilon}\right), \qquad u_s = \sqrt{\frac{2k}{3}} \tag{3.14}$$

In Equation 3.14, two new parameters c_τ and c_ℓ are introduced. These parameters are constant and will be taken from the relevant literature [21].

Substituting all the parameters of Equation 3.14 into the original Equation 3.12 leads to Equation 3.15.

$$\mathrm{d}S(x,\omega) = \frac{A^2 c_l^3 \pi^2}{c_\tau^3 9\rho_0 c_0^5 x^2}\left\{\rho_s^2 k^{7/2}\left(\frac{\omega}{\omega_s}\right)^4 \exp\left(-\frac{\omega^2}{4\omega_s^2}\right)\right\}\mathrm{d}V \tag{3.15}$$

Equation 3.15 is the final form of the formula used for the model from a theoretical point of view. It provides the contribution to the sound radiation of the turbulent structure in a small volume given its

turbulence characteristics.

Below, a small summary of the model parameters is given for reference:

- **Inputs**:
  - x: Distance from the nozzle exit
  - ω: Frequency (concerning the acoustic frequency in the far field)
- **Constants**:
  - A: Turbulence correlation amplitude
  - c_l: Constant related to the length scale in the $k-\epsilon$ RANS model
  - c_τ: Constant related to the time scale in the $k-\epsilon$ RANS model
  - ρ_0 and c_0: Reference density and speed of sound (normal ambient conditions assumed in this case)
- **Variables**:
  - ω_s: Characteristic frequency scale inside the volume $\mathrm{d}V$ (concerning the hydrodynamic frequency of the structures inside the flow)
  - ρ_s: Characteristic density scale inside the volume $\mathrm{d}V$
  - k: Characteristic kinetic energy scale inside the volume $\mathrm{d}V$

This marks the end of the theoretical modelling and assumptions taken directly from literature ([21]) and the predictive model developed in this thesis is henceforth presented.

3.2. The prediction model

Given the entire derivation explained in the previous section, it is not hard to understand that the workflow cannot simply be reversed to achieve the opposite outcome. For that reason an iterative methodology will be used, utilizing the forward methodology of the previous section and applying an iterative optimization technique with experimental data as the target.

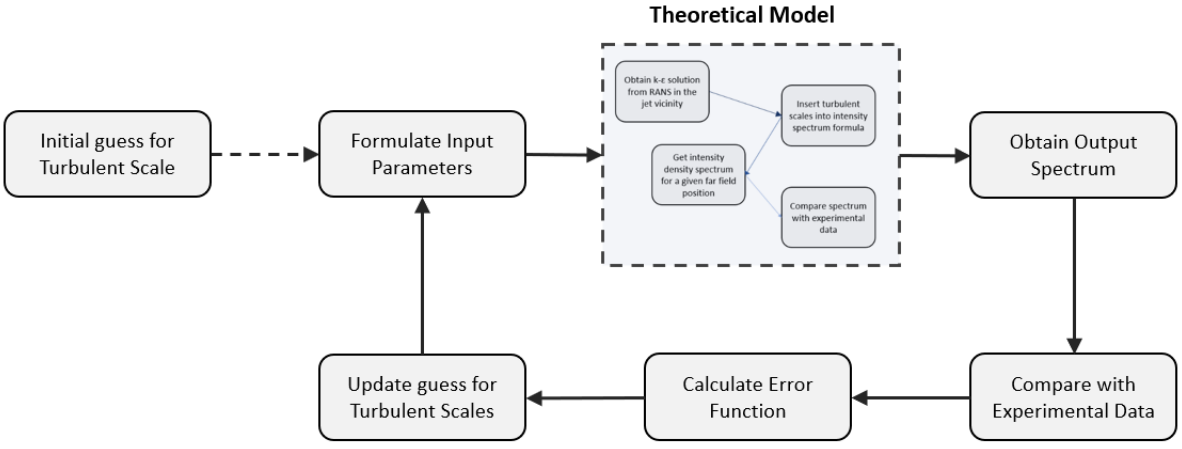

Figure 3.1: Diagram depicting the developed iterative workflow of the noise-source identification model.

Figure 3.1 qualitatively visualizes the iterative nature of the prediction model. It comprises a tailored guess aiming to initiate the process and an iterative loop that, given the input, obtains the output from the theoretical model and after comparing with experimental data, updates the input to the theoretical

model. Each of the blocks shown in Figure 3.1 will be explained in detail below.

3.2.1. Mathematical model simplification

Since the problem at hand is one regarding iterative optimization, it is necessary to formulate it in a way that is computer-friendly, meaning that it is simplified enough such that the iterations and the fitting to experimental data is not computationally expensive. The first step is to simplify Equation 3.15.

Firstly, one needs to understand which parameters will be part of the iterative optimization and which will be the constant inputs. Below a description is given, making a distinction between variables existing in the loop as constant inputs and variables free to be optimized by the algorithm:

Constant Optimization Inputs

- $A\ [-]$
- $c_l\ [-]$
- $c_\tau\ [-]$
- $\rho_0\ [kg/m^3]$
- $\rho_s\ [kg/m^3]$
- $c_0\ [m/s]$
- $x\ [m]$

Variable Optimization Inputs

- $\omega_s\ [rad/s]$
- $k\ [m^2/s^2]$

Function Variable

- $\omega\ [rad/s]$

Note that the distance from the nozzle exit is stated as a constant input since from now on the analysis will be done for a specific far field location, namely 72 jet diameters away from the jet axis (at 90 degrees), in order to correspond to the experimental data presented in literature [21] [23]. In the paper, $D_j = 0.0505m$, resulting in $x = 3.65m$. Moreover, in order to increase the simplicity of the model, it will be assumed that the characteristic density of the flow is equal to the ambient density, reducing the amount of optimization variables from 3 to 2. Overall we are dealing with subsonic jets and especially for low Mach numbers the compressibility effects are minimal. Of course, for the ambient air variables the model uses $\rho_0 = 1.225kg/m^3 (= \rho_s)$ and $c_0 = 343m/s$. The value of the model parameters A, c_l and c_τ will be taken as in the work of Morris and Farassat where they state the following values for the combination of the coefficients: $A^2 c_\ell^3 = 0.0193$ and $c_\tau = 1.43$.

Noticing the amount of constant inputs to the optimization, it is sensible to group all of the into a single one as follows:

$$C_1 = \frac{A^2 c_l^3 \pi^2}{c_\tau^3 9 \rho_0 c_0^5 x^2} \rho_s^2 \tag{3.16}$$

This transforms Equation 3.17 into Equation 3.17 as seen below.

$$\mathrm{d}S(\omega) = C_1 \left\{ k^{7/2} \left(\frac{\omega}{\omega_s} \right)^4 \exp\left(-\frac{\omega^2}{4\omega_s^2} \right) \right\} \mathrm{d}V \tag{3.17}$$

At this point, a discussion needs to be made regarding the choices for ”volumes” to be used for the calculation of the overall spectrum in the far field. In the ideal case, the model would utilize the maximum number of volumes, each volume with a corresponding kinetic energy k and characteristic frequency ω. Each one of those turbulent volumes dV would result in a contribution dS to the overall spectrum and finally all the contributions would be summed up into the final sound intensity density function S(ω) (remember that the current model was set for a specific far field location $x = 72D_j$ for the sake of comparison with experimental data). To avoid diverging from the fundamental purpose of the thesis,

not much attention was paid to the exact choice of the volumes, however, as seen later in Figure 3.3, already for 2 and 3 number of volumes used the spectrum seems to be close (MSE error of less than 1dB) to the experimental one signifying no need for an excessive number of volumes.

Moreover it was assumed that most of the structures are contained within 15 jet diameters downstream and a 5x5 box was taken as the relevant surface in the azimuth. This results in a volume of 15x5x5 jet diameter volumes (D_j^3). For the rest of the analysis the parameter V_{tot} will be introduced representing the relevant jet volume for the purpose of substituting dV since $dV = \frac{V_{tot}}{N}$, under the assumptions that the volume is divided into equal parts.

Adding this relation to Equation 3.17 and taking $\Omega = \frac{\omega}{\omega_s}$, one ends up with Equation 3.18.

$$\mathrm{d}S(\omega) = \frac{C_2}{N} k_i^{7/2} \Omega_i^4 \exp\left(-\frac{\Omega_i^2}{4}\right) \tag{3.18}$$

with (note the addition of V):

$$C_2 = \frac{A^2 c_l^3 \pi^2 V}{c_\tau^3 9 \rho_0 c_0^5 x^2} \rho_s^2 \tag{3.19}$$

The final expression for the overall noise spectrum, ready to be incorporated into an optimization algorithm, is shown in Equation 3.20.

$$S(\omega) = \sum_{i=1}^{N} \frac{C_2}{N} k_i^{7/2} \Omega_i^4 \exp\left(-\frac{\Omega_i^2}{4}\right) \tag{3.20}$$

with C_2 constant, N a chosen small integer and k_i and Ω_i the free variables to be adjusted during optimization in order to provide the best fit to experimental data.

3.2.2. Fitting and optimization

As described before, the algorithm's purpose is to optimize the input variables k and Ω such that Equation 3.20 results in a spectrum as close to that found in literature using real-life data. This required an error function to be created and fed into the optimization as an error minimization problem. Since the goal is to understand which scales are responsible for the largest noise emissions, it was sensible to focus on the points with the most intensity on the spectrum. It was chosen to only take into account the 10 points with the highest intensity in the error calculation since they are the most relevant. Note that throughout this analysis, the data are sampled at specific frequencies.

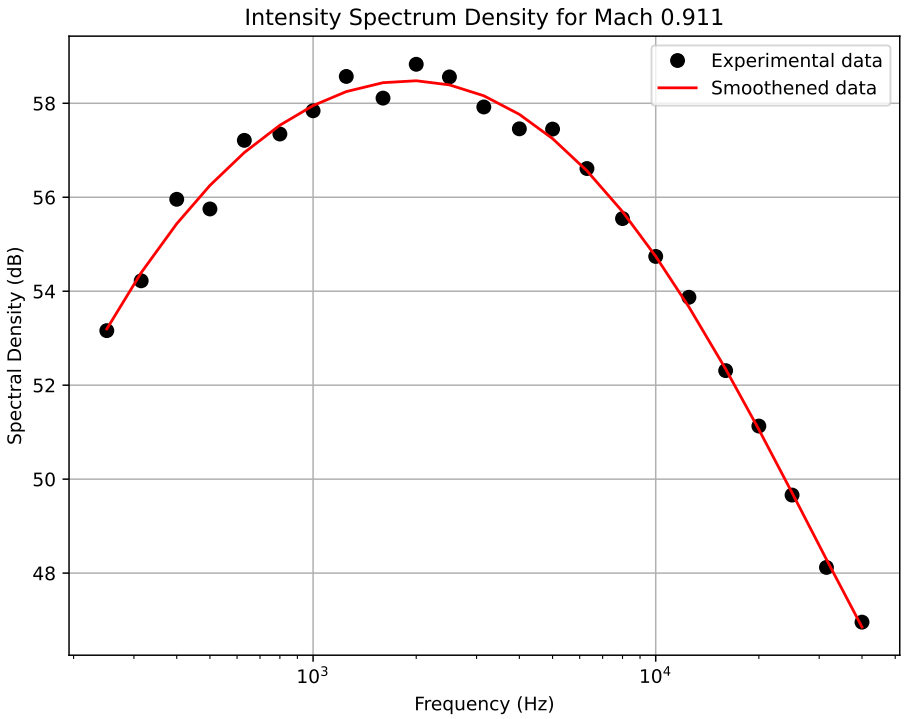

Figure 3.2: Noise spectrum from experimental data ([23]) and their smoothened version.

Figure 3.2 shows an example of a spectrum created from the experimental data of Tanna et al. and a smoothened version which should provide a more representative view of how the spectrum should look like in reality [23]. In this case, the algorithm would utilize the 10 highest points. Note the spectral density unit dB represents in actuality the sound intensity density ($W/m^2/Hz$) which is then normalized by $10^-12 * W/m^2/Hz$ to put it in the dB scale.

The error function is then calculated as the mean squared error of the experimental vs the model calculated intensity at the selected highest points, as shown in Equation 3.21. Note that the np.mean is there for the sake of simplicity signifying that an average of the error is taken for all 10 chosen points.

$$MSE = \sqrt{np.mean(S_{model} - S_{exp})^2} \tag{3.21}$$

Optimization Algorithm

Based on the above cost function, an optimization routine was chosen to minimize the deviation of the estimation from the experimental data. The Nelder-Mead algorithm was chosen since it showed the best and fastest convergence empirically.

To optimize the convergence, the search space of the algorithm was restricted based on physical insights of the two parameters. Regarding the frequency input in the model, it was chosen to restrict the search of ω_s from 0 to 100kHZ (resulting in an effective frequency search space from 0 to 16kHz) since higher values of frequency were irrelevant for the problem at hand. Regarding the limits for the kinetic energy, the bounds were set from 0 to 1000 m^2/s^2 since it was observed that for the high subsonic jet

case of approximately Mach 0.9, the energy required was at max 900 m^2/s^2. Finally, for a better kick-start to the algorithm, the initial guesses for the frequencies ω_s were linearly spread from 1 to 1.5kHz in order to more easily converge to different locations of the frequency spectrum.

Based on those limits and initial inputs, the Nelder-Mead algorithm (which is the standard chosen optimization routine from scipy.optimize module) would follow the flow shown in the diagram of Figure 3.1 until it converged to a stable solution. It would start with the initial inputs described previously which would kick-start the loop by formulating input parameters expected to be close to the end solution. With this input the theoretical model would calculate the output sound intensity density spectrum in dB with is the compared to the experimental data of the given jet [23]. Using the cost function of Equation 3.21 the error would be calculated and used by the Nelder-Mead algorithm to update the guesses for the turbulent scales of the specific jet flow. These guesses would then be the input to the next iteration of the optimization routine until convergence is reached.

3.3. Example Demonstration & Results

In this section an example demonstration of the model procedure leading to the final result will be given for a Mach 0.911 jet (as the one presented in the reference paper [21]) and the results for various Mach numbers will be summarized in the form of required velocity fluctuations at a specific frequency range.

Required energy/frequency for a Mach 0.911 jet

The optimization routine explained in the previous section is performed for a Mach 0.911 jet and the resulting optimized output spectrum is shown using 1, 2 and 3 volumes for the reconstruction at Figure 3.3. In this case, the number of volumes is expressed by the letter m. Again, the reference data are the smoothened version of the experimental data by Tanna et al. [23].

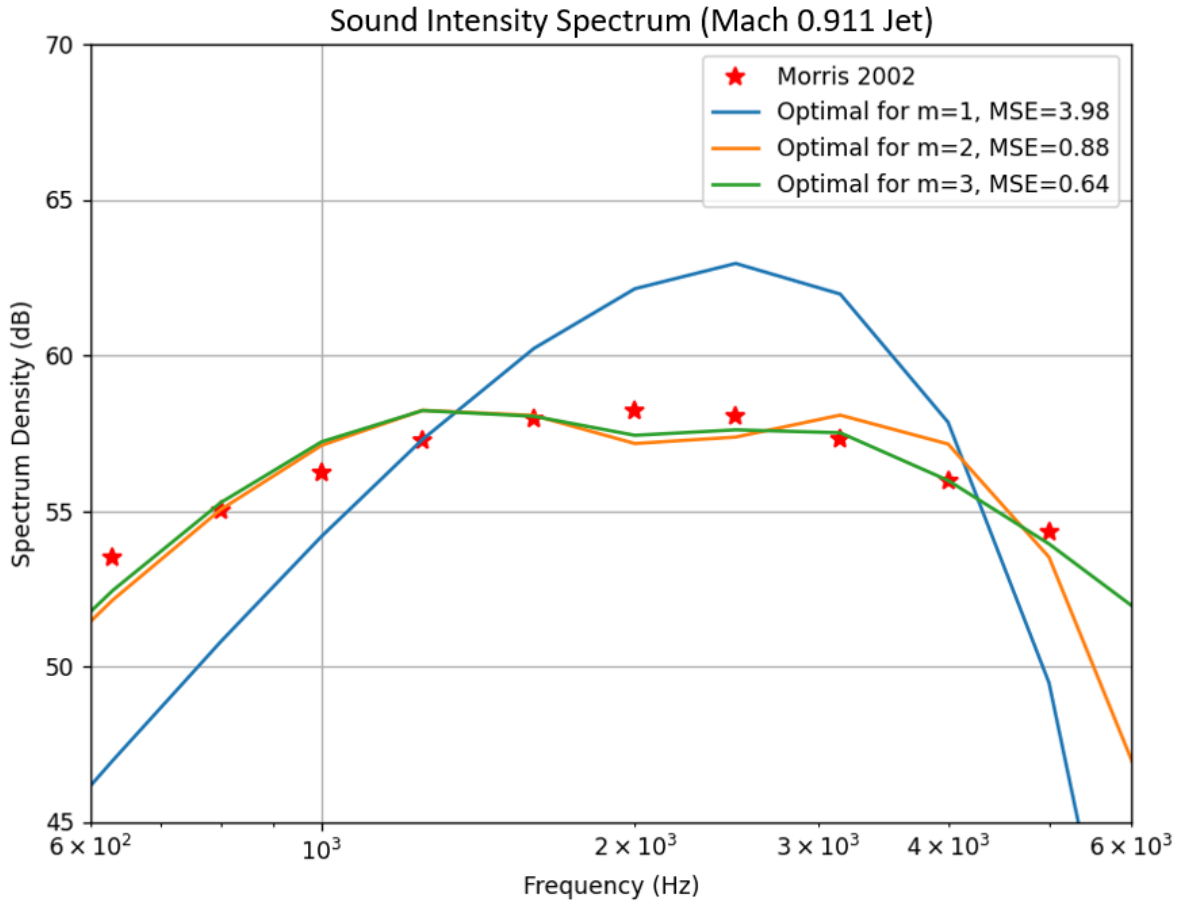

Figure 3.3: Sound intensity spectrum from optimizer for different number of volumes m vs experimental data from Tanna et al.([23]).

Figure 3.3 shows how already with 2 volumes corresponding to two pairs of frequencies and kinetic energies the output spectrum closely matches the experimental data at the peak of the spectrum (10 highest intensity points) with a mean squared error of less than 1 dB for m=2. With a mean squared error of only 0.64 dB for m=3 (corresponding to 6 optimization parameters) and given that the algorithm becomes exponentially more expensive with every additional of volumes, the resulting optimization parameters can already be taken and analysed.

For the sake of simplicity, given that the point of interest is a general range of structures to be targeted by the actuator, the case for m=2 is taken. Below, the converged values of ω_s and k are given in Table 3.1.

	Frequency ω_s $[rad/s]$	Kinetic Energy k $[m^2/s^2]$
Converged Pair 1	2472	665
Converged Pair 2	7645	686

Table 3.1: Frequency and energy values results from optimization.

The values of Table 3.1 are transformed into actual frequency and velocity perturbations using $f_s = \omega_s/2\pi$ and Equation 3.13 (assuming for simplicity's sake that the turbulent kinetic energy is driven by the velocity fluctuations on only one of the three axis) respectively.

Results for a subsonic jet

The procedure described above is performed for jets with a range of subsonic Mach numbers and the results for the range of interest in terms of frequencies and velocity fluctuations are obtained. Just to

refresh the objective, these frequency and velocity scales dictate the space of existence of the turbulent structures that are found in the jet and that associate with the peak of the sound intensity under the assumptions of the theoretical model. This statement therefore indicates that these frequency and velocity scales are the ones necessary to be injected into the flow by some actuation if one wants to alted the flow properties associated with the highest noise intensity in the farfield. Table 3.2 presents the results of the full analysis of the jets with different Mach numbers ranging all inside the subsonic spectrum.

Mach Number	Low f_s $[Hz]$	High f_s $[Hz]$	Low u' $[m/s]$	High u' $[m/s]$
0.353	182.1	451.4	10.3	10.8
0.405	224.6	557.2	11.4	11.8
0.512	247.8	767.0	14.5	14.8
0.621	308.8	953.9	17.7	17.9
0.741	313.1	961.4	20.9	21.4
0.858	390.1	1187.7	23.9	24.0
0.911	393.5	1216.8	25.8	26.2

Table 3.2: Table with Mach Number and Corresponding Frequencies and Velocities

As pointed out before, these results represent the flow scales that correspond to the peak of the sound intensity and henceforth pose the range of the required actuation parameters for the purpose of noise mitigation.

A close look at Table 3.2 leads to the following observations:

- For jets with larger Mach number a higher actuation frequency is required.
- For jets with higher Mach number the required velocity perturbations are higher
- The range of actuation frequency required for a given jet is relatively high (~300-800 Hz)
- The range of velocity perturbations required for a given jet is relatively low (~0.5m/s)

Based on these observations and for the sake of visualization, Figure 3.4 was constructed. It features the energy requirement in terms of mean velocity perturbations at the required frequency range for the different subsonic jets. Note that the velocity perturbation requirement is given as a single number since the range of min to max required is low and so the mean of the low and high u' is highlighted.

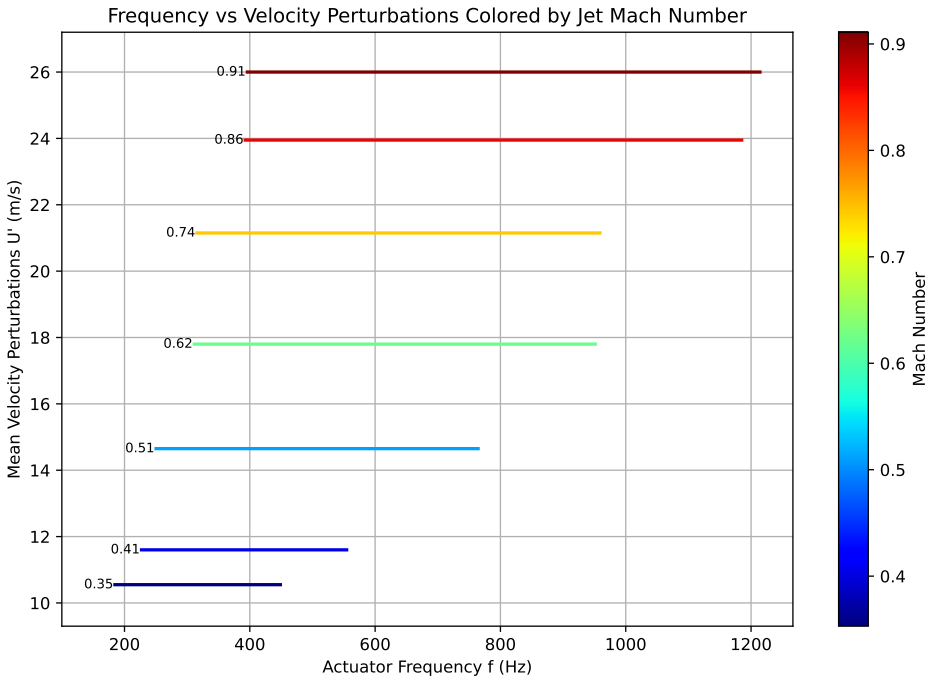

Figure 3.4: Required actuator velocity perturbations for a given frequency range for jets of different subsonic Mach numbers.

Figure 3.4 shows the increase in energy/frequency requirement for increasing Mach numbers. With a quick look, one can see an expected almost linear increase in mean velocity perturbations as well as low and high limits of the frequency window for each increase in Mach number. With this visual hint, it was decided to non-dimensionalize those 3 values. This is done in Table 3.3 where the mean velocity perturbations are given as a percentage of the jet exit velocity and the frequency window limits are replaced with the Strouhal number based on Equation 3.22.

$$\text{St} = \frac{fd}{U_j} \tag{3.22}$$

Here the nozzle diameter d $(= 5.08cm)$ is used as the relevant length scale and the jet exit velocity as the relevant velocity scale calculated as the product of the ambient speed of sound α_0 with the relevant jet Mach number M_j.

Mach Number	Mean u' (%)	St - Lower limit [-]	St - Higher limit [-]
0.353	8.7	0.076	0.189
0.405	8.4	0.082	0.203
0.512	8.3	0.072	0.221
0.621	8.3	0.073	0.227
0.741	8.0	0.063	0.192
0.858	8.0	0.067	0.205
0.911	8.3	0.064	0.197

Table 3.3: Required velocity perturbations as a fraction of the jet velocity and limits of required Strouhal numbers for the different Mach jets.

Table 3.3 perfectly summarizes the actuation requirements for the different jets. It is clear that after the non-dimensionalization the requirements take very similar values and so a general statement can be created based on the average of the limits for the different Mach jets:

- **Frequency requirement:** For a subsonic jet the frequency range required for successful actuation lies approximately between the following limits in terms of Strouhal number:
  - **Strouhal number Low Limit: 0.07 [-]**
  - **Strouhal number High Limit: 0.2 [-]**
- **Energy requirement:** According to the model, for a subsonic jet the velocity perturbations required to be introduced into the flow for successful actuation are:
  - **8.3% of the jet exit velocity**

These energy/frequency requirements henceforth define the actuation space and will be used in the next chapters as the basis for the choice and design of actuators. It needs to be noted that these numbers are subject to various assumptions and simplifications summarized below and therefore may not describe the requirements very accurately. However, they give a good direction for design.

3.4. Limitations

This final section summarizes the assumptions made throughout this modelling and discusses the limitations caused by those assumptions as well as by the methodology followed.

- **Axisymmetric Assumption:**
  - The model assumes an axisymmetric jet, which makes it inapplicable for different types of jets. It may also not fully capture the complexities of real jet flows that can exhibit asymmetric behavior.
- **Far Field Assumption:**
  - The analysis is performed assuming the observer is far from the jet source, simplifying the problem (**x** - **y** = **x**) which results in missing some small near-field noise contributions caused by the different time delay.
- **Equal Characteristic Length Scales:**
  - The model assumes equal characteristic length scales (l_s) in all three spatial directions, which is not expected to be accurate for all turbulent structures in the jet.
- **Gaussian Form of Correlation:**
  - The two-point cross-correlation function is assumed to have a Gaussian form, which simplifies the mathematics but might not represent the true nature of turbulent correlations accurately for all types of jets.
- **Fixed Observation Angle (90 Degrees):**
  - The model focuses on noise prediction at 90 degrees to the jet axis, which is not the angle of maximum noise emission. At different angles an extra step would be required in the approach.
- **Characteristic Density Equal to Ambient Density:**
  - The characteristic density (ρ_s) is assumed to be equal to the ambient density (ρ_0), which holds for low subsonic jets but may not be valid for high Mach number jets where compressibility effects are significant.
- **Limited Number of Volumes:**

  - The optimization uses up to 3 volumes for simplicity and computational efficiency, which might not capture all relevant turbulent structures contributing to the noise.

- **Assumption of Noise Sources Corresponding to Peak Spectrum:**
  - The model assumes that the frequencies corresponding to the peak of the noise spectrum are the most noise-causing. However, it is noted in some literature that the actual noise sources may not always correspond to the peak of the noise spectrum, indicating uncertainty in the theory behind noise sources [8].

These limitations highlight areas where the model's assumptions and simplifications impact its accuracy and applicability. That being said, they suggest directions for future improvements and more comprehensive modeling approaches as will be highlighted in the last section of the report concerning discussions and suggestions about the future of the project.

4

Flow Control

Synthetic Jet Actuators (SJAs) are a prominent example of active flow control devices that import kinetic energy into a flow without any mass addition. They generate jets of fluid by recurrent suction and injection of flow with net-zero mass addition to the system, making them highly efficient for various control applications. This chapter will cover the working principles of SJAs in the context of general flow control, their different types, and the reasons why they are particularly suitable for the specific frequency and energy requirements of the current subsonic jet flow control [3] [35].

In this chapter, firstly the principles and mechanisms of active flow control will be examined, exploring the different concepts and techniques that have been employed throughout the years. Notable examples of active flow control strategies will be given along with their effectiveness, and their applications, always in the context of jet flow control. Special attention will be given to the active flow control using the concept of the synthetic jet creation by actuators of various types, since this will be the flow modification technique utilized in this thesis project.

4.1. Active Control

As mentioned, given its freedom to control the flow in real time, active flow control will be the one of interest. It involves the use of energy inputs to dynamically influence the behavior of fluid flows and in the case of this thesis it will be used to insert kinetic energy with a specific frequency in the jet flow.

4.1.1. Summary of actuators for active flow control

In general, the different types of actuators used for active flow manipulation are generaly divided into four categories based on their function. A great review by Cattafesta and Sheplak lists the different actuation techniques and below a summary is given of the different types [38].

- **Fluidic Actuators**
  - Zero-Net Mass Flux or Synthetic Jets: These actuators create jets by alternating ejection and suction of fluid through an orifice, achieving momentum transfer without net mass addition. Synthetic jets are commonly used for flow control in various aerodynamic applications, enhancing mixing, reducing drag, and delaying flow separation.
  - Nonzero Mass Flux Actuators: These include steady and unsteady jets that introduce additional fluid into the system. Steady jets continuously inject fluid, influencing the flow over surfaces to control separation and reduce drag. Unsteady jets, such as those produced by oscillators and valves, periodically inject fluid, which can be tuned to specific frequencies to disrupt turbulent structures and control flow characteristics.
- **Moving Surface Actuators**
  - Vibrating Ribbon and Flap: These actuators use flexible surfaces that vibrate at specific

frequencies to interact with the flow. Vibrating ribbons and flaps can be used to generate small perturbations in the boundary layer, which helps to control turbulence and delay flow separation.

  - Oscillating Wire and Rotating Surface: Oscillating wires create disturbances in the flow through periodic motion, while rotating surfaces use continuous motion to manipulate the boundary layer and control separation. Both methods are effective in modifying the flow structure around aerodynamic surfaces.
  - Morphing Surface: These actuators alter the shape of the surface dynamically to adapt to changing flow conditions. Morphing surfaces can optimize aerodynamic performance by controlling the flow over wings, blades, or other surfaces, reducing drag and enhancing lift.

- **Plasma Actuators**
  - Corona Discharge: This technique uses high-voltage electrodes to ionize the surrounding air, creating a corona discharge that can induce flow motion and manipulate boundary layers. It's effective in controlling separation and reducing drag.
  - Dielectric Barrier Discharge (DBD): DBD actuators use alternating current to create plasma between electrodes separated by a dielectric barrier. This generates a body force that can accelerate the flow near surfaces, controlling separation and turbulence.
  - Local Arc Filament and Sparkjet: These plasma actuators create high-energy discharges that generate localized jets or shockwaves, influencing the flow structure and controlling turbulence. Sparkjets, in particular, can produce strong, pulsed jets for active flow control.
- **Other Actuators**
  - Electromagnetic Actuators: These actuators use magnetic fields to induce currents in conductive fluids, creating Lorentz forces that alter the flow. They are particularly useful in liquid metal flows and can be applied to control boundary layers and turbulence in gas flows.
  - Magnetohydrodynamic Actuators: Similar to electromagnetic actuators, these use both magnetic and electric fields to control the flow of conducting fluids. They are effective in specialized applications, such as controlling the flow of ionized gases in propulsion systems.

The previous summary provides a useful map of the existing actuators based on their type of function. Now, two important manipulation methods will be presented below based on the physical mechanism they utilize to insert energy into the flow.

- **Acoustic Control**: Acoustic control utilizes sound waves to influence the behavior of turbulent jets. This method has been employed to reduce noise and enhance mixing efficiency in jet flows. Ginevsky et al. [46] demonstrated the effectiveness of acoustic control in turbulent jet applications, showcasing its potential to manipulate flow structures and suppress noise. The acoustic waves can be created by some form of actuation as described above.
- **Active Control of Instability Waves**: Instability waves as discussed in the previous chapter are naturally induced inside jet flows and the amplification of flow structures they can provide can be utilized for flow control. The main concept is to introduce disturbances in the boundary layer where the instability takes place with the expectation that the disturbance will get amplified further downstream and interact effectively with the flow. Controlling instability waves in fluid flows can significantly enhance stability and reduce undesirable oscillations downstream that can be the cause of noise in the far field. Belyaev et al. [50] discussed strategies for active control of instability waves, highlighting the superiority of active methods over passive ones. This approach involves the use of actuators to suppress natural instabilities in a narrow frequency band, as demonstrated by Kopiev et al. [14, 13]. In fact, in one of the recent attempts of Kopiev et al., for the first time there was demonstration of suppression of the naturally induced instability waves of the jet however only in a narrow targetted frequency band [14]. Even though this effort did not manage to reduce the overall sound levels in the far field, it represented a significant achievement when it comes to changing the noise signature of the jet.

Depending on the type of actuation and the physical mechanism utilized, different strategies exist when it comes to placement and control of the actuator. Regarding the placement of the actuator relevant to

the jet, Faranosov et al. emphasized the importance of optimal excitation by actuators near the nozzle edge for effective instability wave excitation [2]. In the paper it is stated how flow manipulation of the boundary layer near the jet nozzle can excite instabilities in the jet shear layer which can be expected to be amplified and interact with the flow. Therefore, near-nozzle actuator placement would be optimal for excitation of instabilities at a certain frequency. Depending on how effective the actuators are on initiating the Kelvin-Helmholtz instability already inside the jet nozzle, the more one can expect to be able to magnify the disturbance and suppress the noise-inducing instabilities with low energy input.

When it comes to active control given a feedback loop, many attempts have been performed to tackle the noise reduction problem. Zhou et al. [54] discussed the possibilities of integrating AI to develop sophisticated control strategies, while Maia et al. [5] recently explored real-time reactive control mechanisms that adaptively respond to changing flow conditions. These all correspond to advanced control technique that involve the use of artificial intelligence inside the loops of the control systems, however it is something beyond the scope of the current project.

4.1.2. Choice of actuator

Since the start of the thesis project, the goal was to utilize synthetic jets for the actuation. Based on the actuation requirements mentioned in the previous chapter, a choice was made regarding which type of actuation should be used. The main considerations were the following:

- Frequency range: The actuator should be able to sustain flow manipulation at frequencies in the order of 1kHz.
- Velocity fluctuations: The actuator should be able to provide fluctuations reaching a peak velocity in the order of 10-20 m/s
- Complexity: The actuator should ideally not require complex technology or complex manufacturing and should be easily reproducible
- Energy requirements: The actuator should not require excess amounts of power to operate

Since many active actuation types revolve around complex technology (for instance corona discharge or electromagnetic actuators), it was chosen to move forward with the simple type of fluidic actuators with zero-net mass addition to the flow. These types of actuators can be utilized to insert momentum without extra mass addition for a small energy cost compared to other actuator types. Below the reasons for using the synthetic jet actuators for this thesis are posed:

- **Minimal Structural Changes/Intrusiveness**: SJAs can be integrated into existing structures with minimal modifications, providing a flexible solution that can be applied to various setups without significant redesign.
- **Low Power Consumption**: SJAs typically consume relatively low power compared to other active flow control methods, making them an energy-efficient option [38].
- **No external fluid source required**: Zero-net mass flux actuators eliminate the need to provide mass/flow from an external source

The main disadvantages usually associated with SJAs are the following [38]:

- **Limited maximum exit velocities to about 100m/s**: Evidently, this limitation does not pose a problem for the current thesis since the actuation area of interest is well below the 100m/s order.
- **SJAs operate at specific frequencies that match the Helmholtz and the structural frequency of the system**: Even though this is considered a disadvantage due to the low frequency range of efficient momentum injection, in the current use case since the range of interest is small these two ”peaks” only help in targeting that range efficiently.

Due to the above reasons and given that the main disadvantages of SJAs do not apply in the case at hand, the SJAs were chosen as the actuation type for the purpose of jet noise control. Following, a more comprehensive description of the SJAs is given.

4.2. Synthetic Jet Actuators

Synthetic jet actuators are devices that generate fluid jets through the periodic ejection and suction of fluid via an orifice, creating vortices and jets without net mass flux, and are widely used in applications such as flow control and noise reduction. In the last section they were selected for the current project given the frequency and energy requirements of the analysis. To summarize, SJAs would be used to try and target structures with a frequency of around the order of 1kHz and at an exit velocity of about 15m/s. In this section the main principles of the synthetic jet creation are explained, focusing on the piezoelectric-driven synthetic jet actuators in specific.

4.2.1. Working Principle

Synthetic jet actuators operate based on the periodic ejection and suction of fluid through an orifice, driven by the oscillatory motion of a diaphragm or membrane. This mechanism results in the formation of jets with no net mass flux, yet significant momentum and energy are imparted to the surrounding fluid. Note that the energy is injected in the form of vortices created at the edge of the orifice due to the continuous ejection and suction of air. This mechanism can be seen in Figure 4.1. One can see the oscillations being driven by a membrane (attached to a piezoelectric element in this case), the cavity and the orifice through which vortices with the driving frequency are being injected forming the synthetic jet. More information is given below.

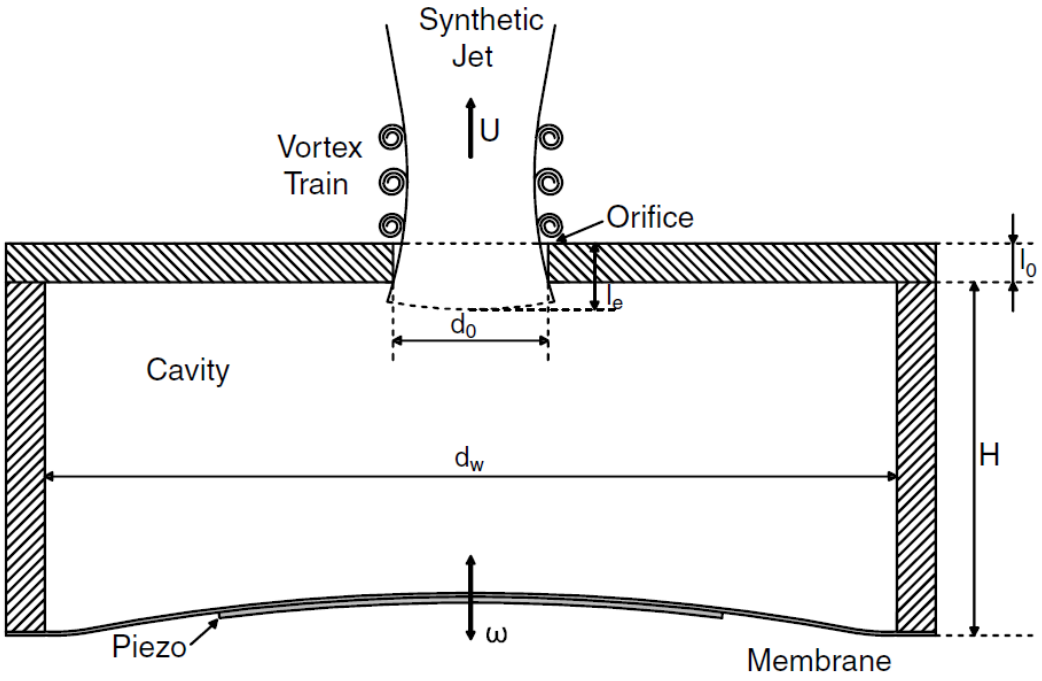

Figure 4.1: Diagram of SJA working principle.

The working principle can be summarized as follows. A vibrational element, such as a piezoelectric actuator, drives the diaphragm to oscillate at a specific frequency. When the diaphragm moves inward (suction phase), it draws fluid into the cavity through the orifice. When it moves outward (ejection phase), it expels the fluid back out through the same orifice. Over one complete cycle of suction and ejection, the net mass of fluid entering and leaving the actuator is zero. Despite this, the periodic ejection of fluid creates vortices at the orifice, resulting in a jet that propagates away from the orifice. During the ejection phase, the expelled fluid rolls up into vortices due to the shear forces at the edge of the orifice. These vortices then interact and merge, forming a coherent jet. The suction phase, conversely, helps in shaping the flow and maintaining the periodicity of the jet formation. Although there is no net mass addition, the created vortices carry momentum and energy into the surrounding fluid. This momentum transfer is responsible for the synthetic jet's effectiveness in various applications ranging from

laptop cooling ([10]), to the flow control for jet noise relevant to this thesis and mixing.

Limitations of synthetic jets

The synthetic jet principle however does not apply for all cases. For instance, a synthetic jet cannot be sustained for very high frequencies. For that reason the jet formation criterion was formed by Holman et al. explaining mathematically for which cases a synthetic jet could be formed [44]. The formation of synthetic jets depends on specific criteria related to the operating conditions and design parameters. Holman et al. outline some basic parameters that affect the formation criterion [44]:

- **Stroke Length**: The stroke length, defined as the distance the diaphragm moves during one oscillation cycle, must be sufficient to produce coherent vortices. If the stroke length is too short, the vortices will not form properly.
- **Frequency of Operation**: The frequency at which the diaphragm oscillates affects the interaction between consecutive vortices. Optimal frequency ensures that vortices are produced at regular intervals and interact constructively to form the coherent jet.
- **Orifice Diameter**: The size of the orifice through which the fluid is ejected plays a critical role in jet formation. A smaller orifice can produce higher velocity jets, but if it is too small, it may restrict the flow and reduce efficiency or even cut the jet completely.
- **Cavity Volume**: The volume of the cavity behind the diaphragm influences the pressure dynamics during oscillation. An appropriately sized cavity ensures that the diaphragm motion generates the necessary pressure changes to produce strong jets.

The jet formation criterion is governed by the Strouhal number (Sr) which relates to the dimensionless parameters Reynolds number (Re) and Stokes number (S) [16]. The experimental data support the criterion expressed in Equation 4.1.

$$\frac{1}{Sr} = \frac{Re}{S^2} > K \tag{4.1}$$

Here the constant K is approximately 1 for two-dimensional jets and 0.16 for axisymmetric jets [44]. This constant K depends on the geometry of the orifice, including the radius of curvature and the aspect ratio of the slot. Since this project is dealing with an axisymmetric jet, during the actual design of the actuator K=0.16 will be used.

4.2.2. Piezoelectric-Driven Actuators

As mentioned previously, the SJA requires some excitation mechanism on one side of the diaphragm that will introduce the oscillations into the cavity and out of the orifice. This can be done by any harmonically vibrating surface for instance a normal piston moving up and down at a specific frequency. In recent applications, three types of actuation are preferred: loudspeakers, piezoelectrics and plasma [17].

Among these, piezoelectric actuators are often chosen due to their ability to operate at the optimal frequency in the order of a 1kHz. Loudspeakers, while capable of providing harmonic motion, typically operate at lower frequencies, often below 500 Hz, which may not be sufficient for applications that require high-frequency oscillations for effective synthetic jet formation [42, 36]. On the other hand, plasma actuators can achieve much higher frequencies, often exceeding several kHz, but they are more complicated to implement. Plasma actuators require high-voltage power supplies and generate thermal effects that can complicate their use in certain environments and applications [17].

Piezoelectric actuators thus offer a balanced solution by providing sufficient frequency for effective jet formation while maintaining a relatively simple and compact design. They also exhibit high precision and rapid response times, which are critical for applications where precise control of jet characteristics could be necessary such as trying to excite the instability waves in the case of this thesis. This could

be useful for the future of the project since precise control will be required possibly in a closed-form. Additionally, piezoelectrics are energy-efficient, making them suitable for use in systems where power availability is a concern. These advantages make piezoelectric actuators a preferred choice in many synthetic jet actuator applications and this is why they are chosen for the sake of this project. Here their main principle is explained in the context of driving the oscillations within the SJA cavity.

Piezo working principle

Here a brief explanation of the working principle of piezoelectric elements is given.

When an electric field is applied to a piezoelectric material, it undergoes mechanical deformation and ,conversely, mechanical stress on the piezoelectric material is able to generate an electric charge. In synthetic jet actuators, this effect is used to convert electrical energy into mechanical motion through the diaphragm. By convention, the piezoelectric material is attached to a metal sheet which vibrates with it producing the driving oscillations for the synthetic jet creation. Together they form the diaphragm which looks as in Figure 4.2.

(a) Piezo diaphragm element

(b) Piezo diaphragm side view

Figure 4.2: Illustration of a conventional diaphragm made up by the piezoelectric ceramic (light grey) and the metal sheet (in this case brass disk depicted in dark yellow).

The disk diaphragm vibrates upon imposing an alternating electric field to the piezoelectric ceramic which expands and contracts, causing the diaphragm to oscillate.

The frequency and amplitude of the diaphragm's oscillations can be precisely controlled by adjusting the electric signal applied to the piezoelectric material. This control allows for tuning all the desirable characteristics of the synthetic jet as discussed previously.

This signal in combination with the cavity geometry form the basis of the actuator. There are several studies like the one by Zhang et al. where the different actuator configurations are tested given different geometrical parameters [30]. The frequency response for the different setups is obtained and compared to understand which parameters are of the most important when it comes to the SJA performance. The equivalent study but driving the SJA using a loudspeaker is also done by Zhang et al. in a previous paper [29].

5

Piezoelectric-Driven Synthetic Jet Actuator Design

This chapter provides a detailed exploration of piezoelectric-driven synthetic jet actuators, focusing on both the theoretical modeling and practical implementation required for this thesis. The purpose of this chapter is to provide insights into the framework followed starting from the energy/frequency requirements of the previous chapters which, combined with a theoretical model, resulted in an optimal actuator geometry which is designed, tested and evaluated.

It begins with the theoretical modeling of synthetic jet actuators, developing a comprehensive model that includes the dynamics of the diaphragm, cavity, and orifice, and formulates a coupled system of equations to describe and predict the actuator's behavior. Following this, the chapter transitions to the practical design of the piezo-driven SJA using the theoretical model to predict the geometry of the SJA that is expected to output the desired frequency response, discussing the key considerations and parameters for achieving these desired performance outputs. Moreover, the manufacturing as well as testing processes used are explained. Finally, the evaluation of the effectiveness of the actuators across different frequencies is presented, showcasing the experimental frequency responses vs the outcomes of the theoretical model.

5.1. Theoretical Modelling

The theoretical formulation used in this section to model the piezoelectric-driven SJA is based on a lumped-element model which considers the piezo-cavity-orifice system as a two-coupled oscilator system, developed by de Luca et al. [31]. The modelling idea was first introduced by Sharma who developed an analytical fluid dynamics based model for actuation with synthetic jets [40]. The piezoelectric element with the vibrating metal surface is modelled as a single degree-of-freedom mechanical system which is in turn coupled with the cavity-orifice system which is analytically modelled using the unsteady forms of the continuity and Bernoulli equations [40]. This basic formulation is used by de Luca et al., the model of which is henceforth explained.

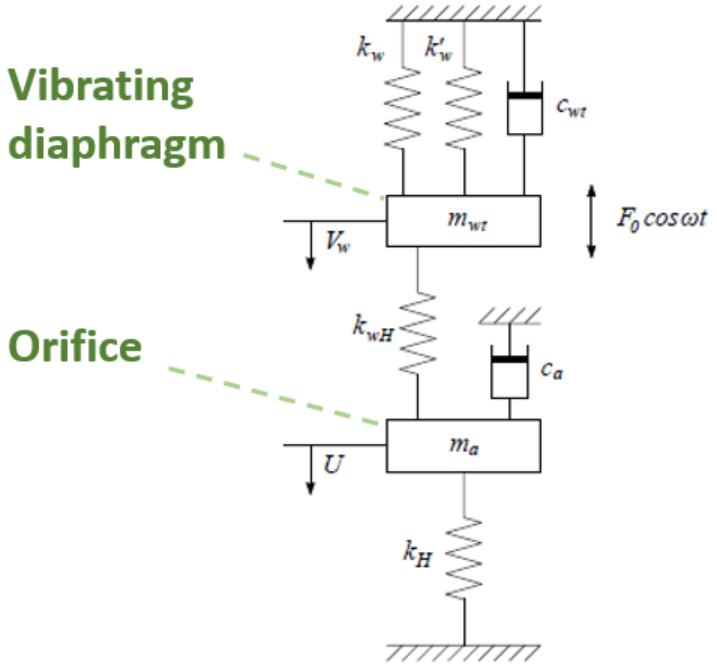

Figure 5.1: Schematic of the coupled oscilator system representing the interaction between the forced vibrating diaphragm and the cavity acting as a Helmholtz resonator (adapted from [34]).

Figure 5.1 showcases the visual representation of the model solution at hand and will be used throughout this section for reference. It depicts the vibrating diaphragm m_{wt} as a component with a forced sinusoidal vibration $F_0 cos\omega t$, stiffness and damping k_w and c_{wt} respectively, moving at velocity V_w. This is coupled to the Helmholtz resonator m_a with the equivalent coupling stiffness k_{wH} coming directly from the system stiffness matrix which will be explained below. This resonator is connected to the geometrical properties of the cavity and the orifice, resulting in stiffness and damping k_H and c_a respectively. The velocity U seen in Figure 5.1 represents the velocity at the orifice and can be considered as the model response.

Having given the context required the modelling, below the derivation is explained using the theory of de Luca et al. which is also concisely summarized by Chiatto et al. in a review paper [31, 34]. Note that the derivation until the final implicit model solution is derived is taken directly from de Luca et al. The personal touches of this thesis are presented later on in the chapter where a manual tuning is performed.

5.1.1. Diaphragm dynamics

The diaphragm, or membrane, is modeled as a single-degree-of-freedom (SDOF) forced-damped spring-mass system. The equation of motion for the diaphragm is given in Equation 5.1.

$$m_{wt}\ddot{x}_w + c_{wt}\dot{x}_w + k_w x_w = F - p_i A_w \tag{5.1}$$

where:

- $m_{wt} = m_w + m_a$ is the total mass, including the diaphragm mass m_w and the added mass m_a term taking into account the mass of the air being displaced upon movement of the membrane ($[kg]$),
- $c_{wt} = c_w + c_a$ is the total damping coefficient, including structural damping c_w and additional damping due to air interaction c_a ($[-]$),
- k_w is the equivalent spring stiffness ($[N/m]$),

- $F = F_0 \sin(\omega t)$ is the electrodynamic force applied by the piezoelectric element ($[N]$),
- p_i is the internal differential pressure ($[Pa]$),
- A_w is the diaphragm area ($[m^2]$),
- x_w is the diaphragm displacement ($[m]$).

The equivalent spring stiffness k_w can be expressed as in Equation 5.2.

$$k_w = m_w(2\pi \tilde{f}_w)^2 \tag{5.2}$$

where $\tilde{f}_w$ is the frequency of the principal mode of vibration of a rigidly clamped disk. It is assumed that this first vibrational mode is dominant and thus equals the overall structural frequency of the clamped disk system.

5.1.2. Cavity dynamics

The continuity equation, under the assumption of an isentropic process, physically relates the internal pressure change to the diaphragm displacement and the orifice flow velocity U. The continuity equation taked the form as seen in Equation 5.3.

$$V_c \frac{1}{\gamma p_0} \frac{dp_i}{dt} - A_w \dot{x}_w = -A_o U \tag{5.3}$$

where:

- $V_c = A_w H$ is the cavity volume ($[m^3]$),
- A_o is the orifice area ($[m^2]$),
- H is the cavity height ($[m]$),
- γ is the specific heat ratio ($[-]$),
- p_0 is the ambient pressure ($[Pa]$).

5.1.3. Orifice Dynamics

The last part of modelling takes into account the dynamics of the orifice. The flow through the orifice is governed by the unsteady Bernoulli equation which is highlighted in Equation 5.4.

$$\dot{U} + \frac{K}{l_e}|U|\dot{U} + \omega_h^2 U = \frac{A_w}{A_o}\omega_h^2 \dot{x}_w \tag{5.4}$$

where:

- K is the head loss coefficient ($[-]$),
- l_e is the effective orifice length ($[m]$),
- $\omega_h = \sqrt{\frac{\gamma A_o^2 p_0}{V_c \rho_a}}$ is the Helmholtz frequency ($[rad/s]$),
- ρ_a is the air density ($[kg/m^3]$).

5.1.4. Coupled System of Equations

The three equations can be summarized as a coupled system:

$$\ddot{x}_w + 2\zeta_w \omega_w \dot{x}_w + \omega_w^2 x_w = \omega_w^2 \Delta x_w \sin(\omega t) - \frac{p_i A_w}{m_{wt}} \tag{5.5}$$

$$\frac{V_c}{\gamma p_0}\frac{dp_i}{dt} - A_w \dot{x}_w = -A_o U \tag{5.6}$$

$$\dot{U} + \frac{K}{l_e}|U|\dot{U} + \omega_h^2 U = \frac{A_w}{A_o}\omega_h^2 \dot{x}_w \tag{5.7}$$

Here, ζ_w and ω_w are the damping ratio and natural frequency of the diaphragm, respectively:

$$\zeta_w = \frac{c_{wt}}{2\sqrt{m_{wt}k_w}} \tag{5.8}$$

$$\omega_w = \sqrt{\frac{k_w}{m_{wt}}} \tag{5.9}$$

For the final complete coupled system representation, the time derivative of Equation 5.5 is taken and the differential internal pressure is replaced with the expression of Equation 5.6. This gives the first of the two equations, considering the coupling of the diaphragm with the cavity. The second equation is Equation 5.7, considering the flow physics of the orifice with respect to the cavity volume. Together they form the final coupled system of equations expressed in Equation 5.10.

$$\begin{bmatrix} \ddot{V}_w \\ \ddot{U} \end{bmatrix} + \begin{bmatrix} 2\zeta_w\omega_w & 0 \\ 0 & \frac{K}{l_e}|U| \end{bmatrix} \begin{bmatrix} \dot{V}_w \\ \dot{U} \end{bmatrix} + \begin{bmatrix} \frac{1}{m_{wt}} & 0 \\ 0 & \frac{1}{m_a} \end{bmatrix} \begin{bmatrix} k_w + \frac{\gamma p_a}{V_c}\frac{A_w^2}{A_o} & -\frac{\gamma p_a}{V_c}\frac{A_o A_w}{A_w} \\ -\frac{\gamma p_a}{V_c}A_o A_w & \frac{\gamma p_a}{V_c}A_o^2 \end{bmatrix} \begin{bmatrix} V_w \\ U \end{bmatrix} = \begin{bmatrix} \frac{F_0}{m_{wt}}\omega\cos(\omega t) \\ 0 \end{bmatrix} \tag{5.10}$$

5.1.5. Solution of the coupled model

The resulting algebraic, non-linear system can be implicitly solved to give the amplification factor of the maximum jet velocity with respect to the incompressible velocity, $U_{\text{inc}} = (A_w/A_o)\omega\Delta x_w$ [34]. The implicit solution is given in Equation 5.11.

$$\frac{U_{\text{max}}}{U_{\text{inc}}} = \frac{1}{\sqrt{\left(2\zeta_w\frac{\omega}{\omega_w} + 2\zeta_U\frac{\omega}{\omega_H}\delta_{\text{CF}}\right)^2 + \left(\delta_1\delta_2 + 4\zeta_w\zeta_U\frac{\omega}{\omega_w}\frac{\omega}{\omega_H}\right)^2}} \tag{5.11}$$

.

Here, the formulation $\delta_{\text{X}} = \left(1 - \omega^2/\omega_X^2\right)$ is used, with X representing other the Helmholtz frequency (X=H) or the coupled oscilator frequencies (X=1 and X=2). The structural frequency through the coupling factor of the two oscilators $CF = \frac{\omega_{wc}^2}{\omega_w^2}$ is also similarly given as $\delta_{\text{CF}} = \left(1 + CF - \omega^2/\omega_w^2\right)$. As described previously, ζ_w and $\zeta_U = (U_{\text{max}}K)/(2\omega_H l_e)$ are the structural and fluid dynamic damping factors respectively and it is visible how Equation 5.11 becomes implicit through ζ_U [34]. Note that some model parameters' explanation is still missing and will be given in the next section as clarifications.

This implicit representation of the solution marks the end of the theoretical derivation taken directly from de Luca and Chiatto. The steps taken henceforth for solving this expression as well as the actual actuator design are exclusive to this thesis.

Iterative solution

Since Equation 5.11 does not have an explicit solution, an iterative solution routine is used once again to converge to a solution. The scipy minimize routine is used with the Nelder-Mead optimization algorithm as the default. An initial guess of $U_{max} = 30m/s$ is used to kickstart the model.

Note that the solution of this theoretical model for a given frequency ω gives the maximum velocity at the orifice. However, in all practical applications given that all the measurements are effectively taken at least an orifice diameter away from the orifice plane, a small transformation is taken to account for the distance as seen in Equation 5.12.

$$U_e = 1.1\frac{U_{\text{max}}}{\pi} \tag{5.12}$$

where U_e is referred to as the ”saddle point velocity” and it is the velocity used for comparisons with experimental measurements of exit velocities.

5.1.6. Parameter summary and clarifications

For clarity, all the input parameters to the model are summarized in Table 5.1 featuring the name, symbol and unit of each input parameter as well as where its value is obtained from.

Parameter Symbol	Parameter Name	Unit	Definition / How to Obtain
γ	Specific heat ratio	-	Property of air
δ_{CF}	Coupling frequency term	-	Conventionally defined as: $1 + \mathsf{CF} - \frac{\omega^2}{\omega_2^2}$
δ_{H}	Helmholtz frequency term	-	Conventionally defined as: $1 - \frac{\omega^2}{\omega_2^2}$
ζ_U	Damping ratio of fluid dynamics	-	Conventionally defined as: $\frac{U_{\mathsf{max}} K}{2\omega_H l_e}$
ζ_w	Damping ratio of diaphragm	-	Defined as: $\frac{c_{wt}}{2\sqrt{m_{wt} k_w}}$
ω_h	Helmholtz frequency	rad/s	Calculated as: $\sqrt{\frac{\gamma A_o^2 p_0}{V_c \rho_a}}$
$\omega_{1,2}$	Coupled resonance frequencies	rad/s	Conventionally defined as: $\frac{\omega_w^2 + \omega_h^2 \pm \sqrt{(\omega_w^2 + \omega_h^2)^2 - 4\omega_w^2 \omega_h^2}}{2}$
ω_{wc}	Pneumatic spring natural frequency	rad/s	Calculated from geometry: $\sqrt{\frac{\gamma A_w p_a}{m_{wt} H}}$
ω_w	Natural frequency of diaphragm	rad/s	Calculated as: $\sqrt{\frac{k_w}{m_{wt}}}$
Δx_w	Diaphragm displacement amplitude	m	See below
Φ_a	Electroacoustic transduction	Pa/V	See below
A_o	Orifice area	m^2	From orifice geometry
A_w	Diaphragm area	m^2	From diaphragm geometry
CF	Coupling factor	-	Conventionally defined as: $\frac{\omega_2^2}{\omega_w^2}$
H	Cavity height	m	From diaphragm geometry
k_w	Equivalent spring stiffness	N/m	Calculated as: $m_w(2\pi \tilde{f}_w)^2$
K	Head loss coefficient	-	Derived from empirical data or fitting
l_e	Effective orifice length	m	From orifice geometry and corrections
m_{wt}	Total mass	kg	Diaphragm mass with added mass from air displacement
m_w	Diaphragm mass	kg	Mass of the shim and the piezo
p_0	Ambient pressure	Pa	Ambient atmospheric pressure
ρ_a	Ambient density	kg/m^3	Density of air at ambient conditions
$\tilde{f}_w$	Shim principle mode frequency	Hz	See below
U	Flow velocity through orifice	m/s	Equation variable
V_c	Cavity volume	m^3	Geometrically calculated as: $A_w H$
V_{ac}	Voltage (alternating current)	V	Signal voltage (model input)
$\mathbf{U_{max}}$	**Maximum jet velocity**	**m/s**	**Model output variable**

Table 5.1: Summary of Input Parameters for the Coupled Oscillator Model of Synthetic Jet Actuators (Ordered by Greek and Latin Symbols)

Here attention is given to some parameters involved in the model the value of which arises through extra modelling, assumptions and experimental tuning.

- **Shim principle vibrational mode frequency** - $\tilde{f}_w$:

  This parameter is estimated using an empirical formula based on the shim parameters as shown below [31]:

  $$\tilde{f}_w = \frac{10.2}{(\pi\sqrt{3})} \left(\frac{t_{\text{shim}}}{d_w^2} \right) \sqrt{\frac{E_{\text{shim}}}{\rho_{\text{shim}}(1-\nu_{\text{shim}}^2)}} \tag{5.13}$$

  Where d_w, ν_{shim}, E_{shim}, ρ_{shim} and t_{shim} represent the diameter, Poisson ratio, Young's modulus, density and thickness of the metalic shim respectively.

- **Diaphragm displacement amplitude** - Δx_w:

  This parameter too utilizes an empirical relation of the diaphragm displacement to piezoelectric ceramic element [31]:

  $$\Delta x_w = \frac{V_{ac}}{A_w} \Phi_a \frac{\pi d_{\text{pc}}^6 \left(1-\nu_{\text{pc}}^2\right)}{1024 E_{\text{pc}} t_{\text{pc}}^3} \tag{5.14}$$

  where d_{pc}, ν_{pc}, E_{pc} and t_{pc} represent the diameter, Poisson ratio, Young's modulus and thickness of the piezoelectric ceramic disk respectively. Φ_a is the electroacoustic transduction and acts as a tunable parameter in the model and V_{ac} is the alternating current voltage applied (also knows as V_{RMS}).

- **Effective orifice length** - l_e:

  This is a parameter used in fluid dynamics to account for the additional length of the orifice that affects the flow behavior. It combines the actual physical length of the orifice with an additional length that accounts for entrance and exit effects as seen below:

  $$l_e = l_0 + \Delta l_e d_0 \tag{5.15}$$

  where l_0 and d_0 are the length and diameter of the orifice and Δl_e is a tunable parameter.

- **Frequencies of the coupled oscilators** - $\omega_{1,2}$:

  Due to the coupling taking place within the system, the Helmholtz as well as the structural frequencies shift. The coupled natural frequencies $\omega_{1,2}$ can be derived from the characteristic equation of the system. Assuming no damping for simplification, the following relation between the frequencies is obtained:

  $$\omega_{1,2}^2 = \frac{\omega_w^2 + \omega_h^2 \pm \sqrt{(\omega_w^2+\omega_h^2)^2 - 4\omega_w^2\omega_h^2}}{2} \tag{5.16}$$

With all these input parameters at hand, the complete model was set up. For the sake of validation, the model was run using experimental data as done in another paper by Chiatto et al. [33]. Evidently, there was a mismatch between the validation data from Chiatto et al. and the data output from the model developed in this thesis. As will be shown in the next section, even the experimental frequency response of the actuator with the same geometry was found to be different, indicating that a more personalized approach should be taken when it comes to the model tuning rather than following all the steps performed by Chiatto et al. The reason for this mismatch was not identified however it can probably be attributed to different the materials and clampings used (metal vs resin) in the two cases of manufacturing.

5.2. Actuator Design

5.2.1. Energy/frequency objective

For the sake of this demonstration, the jet presented in the paper by Morris and Farassat is taken as reference with a nozzle diameter of 0.0508m, since the Tanna's experimental data describe that particular jet geometry [21, 23]. For the demonstration of the SJA working principle it was chosen to

target a Mach 0.5 jet and in particular the higher relevant frequencies due to actuator limitations. These choices result in the energy/frequency target space as highlighted in Figure 5.2 in yellow.

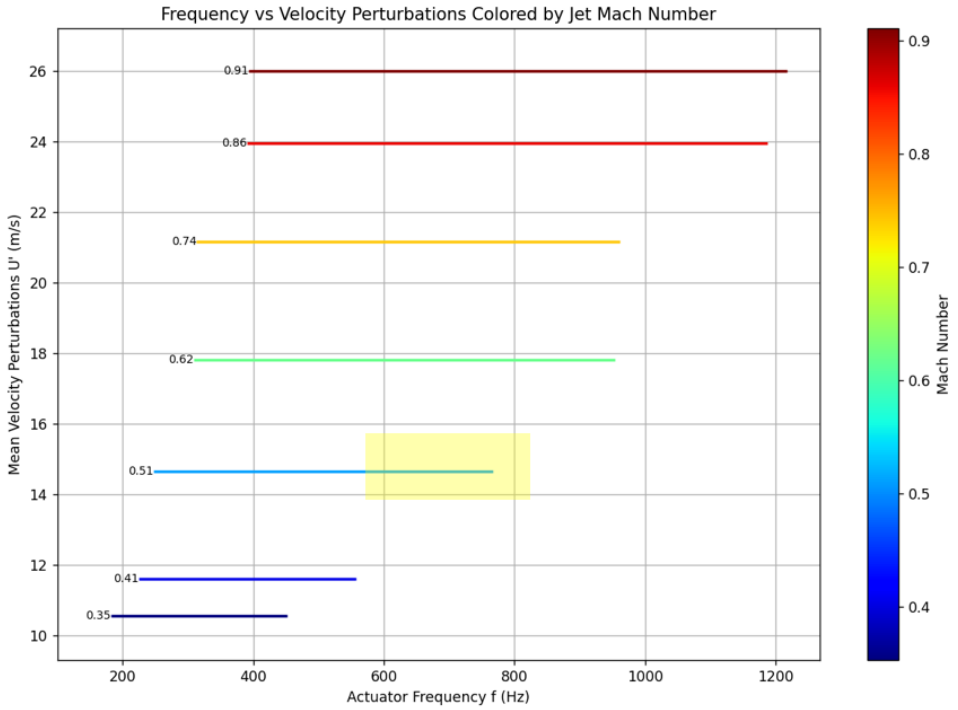

Figure 5.2: Actuator objective in terms of velocity perturbations vs frequency range for a jet with $d_j = 0.0508m$.

To quantitatively summarize the objective based on the graph of Figure 5.2:

The actuator should have the capability to provide velocity fluctuations reaching a U_{max} of approximately 15m/s at a frequency ranging from 600 to 800Hz.

Moreover, the ideal actuator would have a flat velocity response at the desired frequency range, as for instance the one presented by Zhang [30].

5.2.2. Model tuning

As mentioned previously, the model tuning by de Luca et al. did not manage to give the same model response while applied in the context of this thesis project. At the same time it is shown how even the experimental data of the exact same geometry do not match. Figure 5.3 demonstrates this mismatch between the experimental data obtained in this thesis vs the data reported by Chiatto et al. [34]. It should be noted that the experiment in this thesis was performed at half the voltage (25Vrms) compared to the one in literature (50Vrms) which should have an impact on the overall amplitude. However, even with this different voltage, the overall shape of the response should be the the same in both cases, something which is not seen in Figure 5.3. For that reason, a manual tuning was performed.

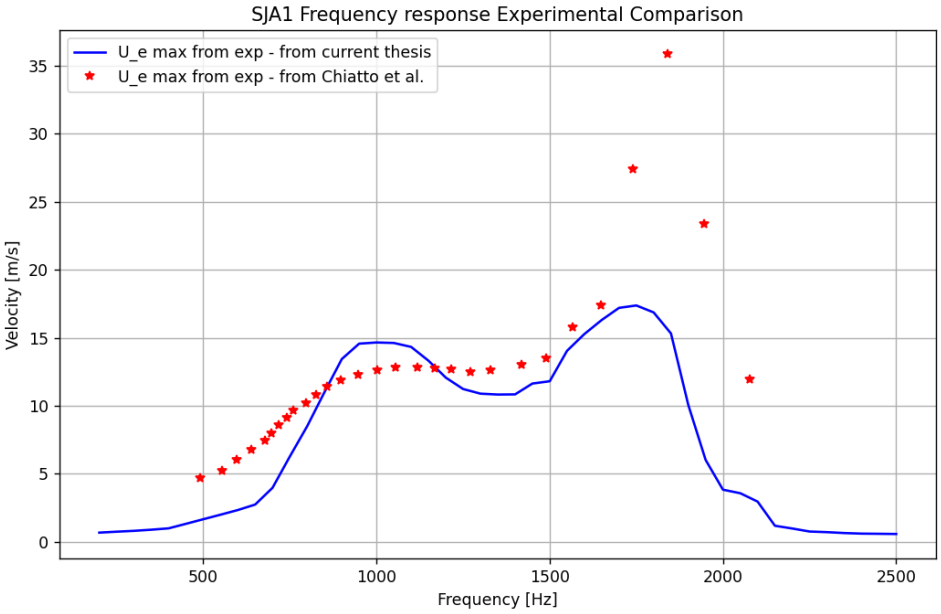

Figure 5.3: Comparison of experimental frequency response obtained in this current thesis vs the results by Chiatto et al. [34] ($d = 41mm$, $H = 1.5mm$, $d_0 = l_0 = 2mm$).

For the tuning, the following geometrical parameters were chosen to define the actuator geometry:

- **Cavity diameter**: 41mm
- **Cavity height**: 1.5mm
- **Orifice diameter**: 2mm
- **Orifice length**: 2mm

These values were chosen based on the frequency response presented by Chiatto et al. at their review paper featuring a brass-shim piezoelectric-driven SJA with a very desirable frequency response (flat velocity response close to 800Hz). This geometry was used as reference for the manufacturing of an actuator built to be tested and then tune the model to fit the experimental data obtained. Only after this 1st iteration tuning can the model be used as reference to predict the responses of specific SJA geometries.

Moving on, a SJA with that exact geometry was manufactured and tested (information regarding those are given in the next sections) providing the following frequency response as shown in Figure 5.4.

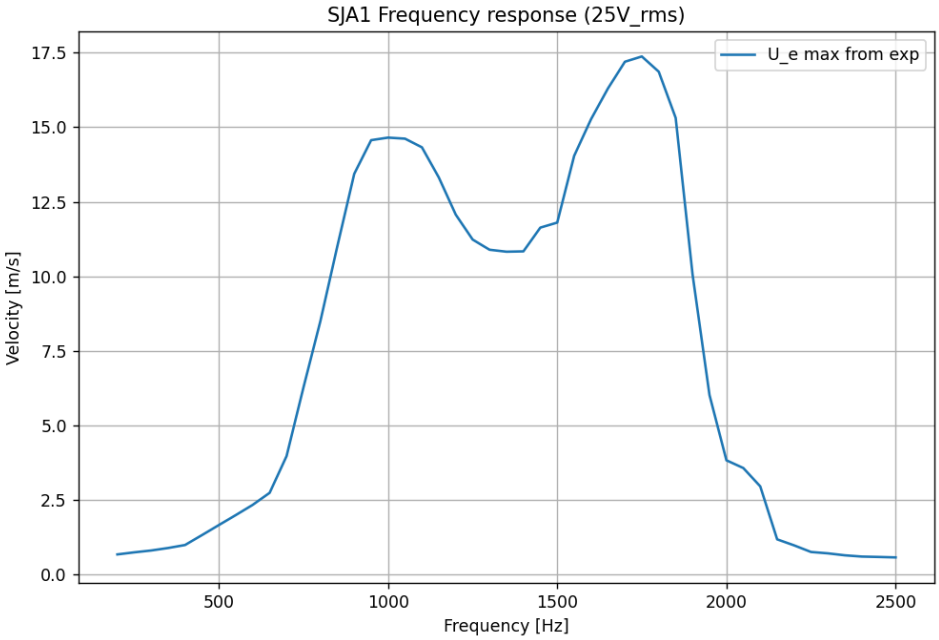

Figure 5.4: Experimental frequency response of piezo-driven actuator with a brass shim ($d = 41mm$, $H = 1.5mm$, $d_0 = l_0 = 2mm$).

These experimental data can now be used to tune the model. For the sake of comparison, Figure 5.5 nicely illustrates the difference in model response between the tuning based on the parameters used by de Luca et al. and the parameters after manual tuning.

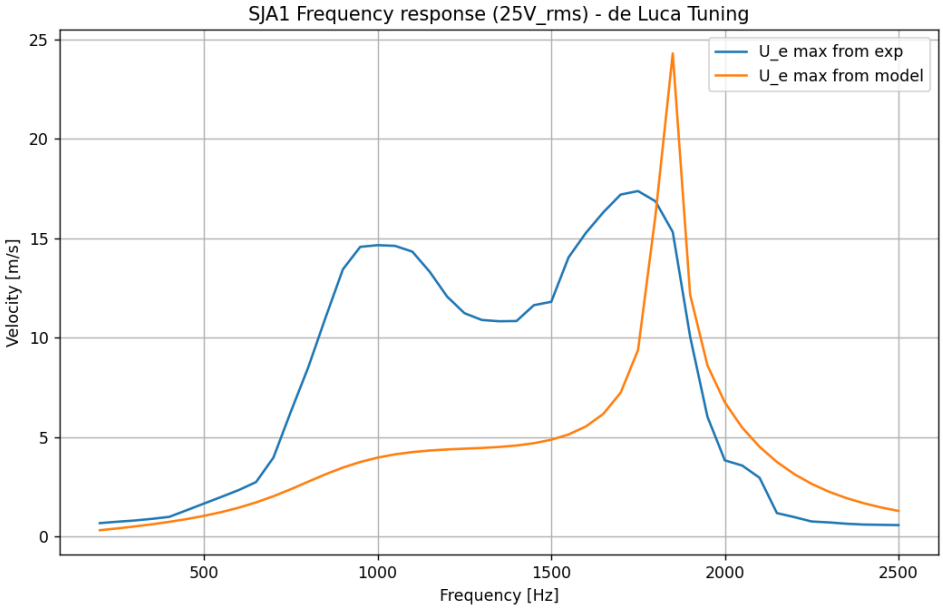

(a) de Luca Tuning

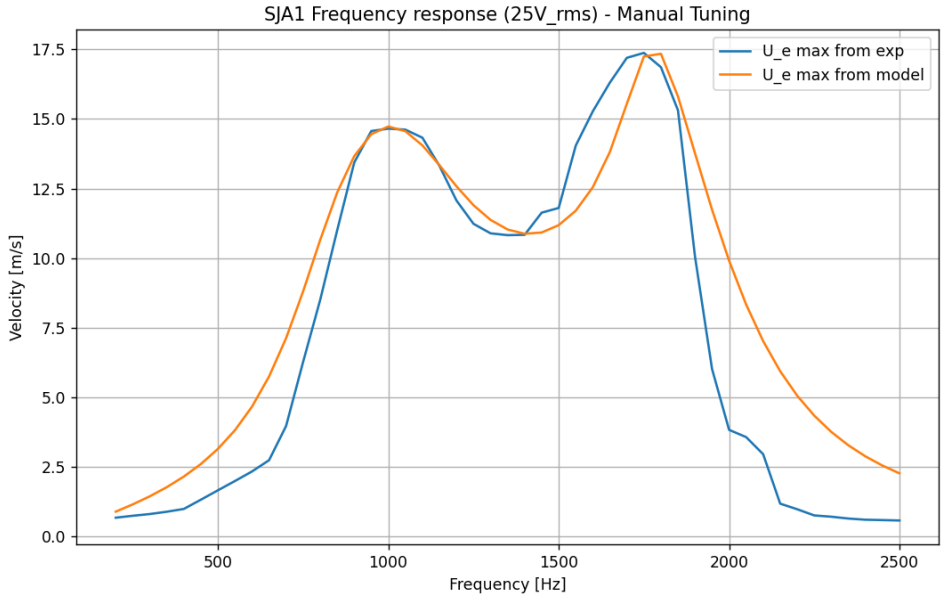

(b) Manual Tuning

Figure 5.5: Experimental data vs model fit using the tuning parameters from de Luca et al. ([31]) and the manual tuning.

As seen in Figure 5.5, the parameters of the initial tuning result in a very high peak response corresponding to the structural frequency compared to the Helmholtz one which is almost flat, an issue which is solved by tweaking the parameters to give more emphasis to the Helmholtz resonance frequency. Due to the complex coupling between tuning parameters and response, no exact tuning logic can be presented and it is admitted that tuning was done on a manual trial-and-error basis. Overall, one can see that after the tuning the model is able to capture the peak frequencies very closely (exact Helmholtz frequency and slightly off model structural frequency) and precisely guesses the height of those peaks. Outside of the resonance frequencies the model is only able to capture the overall behaviour without much precision which, however, is not required since the area of importance is that close to the resonance frequencies.

Table 5.2 showcases the values of the tunable model parameters before and after the manual tuning.

Parameter Name	Before tuning	After tuning
K	1.14	0.225
Φ_a	105	290
Δl_e	0.62	1.2
ζ_w	0.03	0.1

Table 5.2: Comparison of model tuning parameters before and after manual tuning

Using the newly tuned parameters the model is now expected to give a more representative actuator response given a geometry.

5.2.3. Desirable actuator geometry

According to the velocity/frequency requirement posed previously, the model is now used to output the four geometrical parameters that define the actuator geometry with the desirable response. Below, this response is shown together with the geometrical parameters of the cavity and orifice that should in theory result in that response.

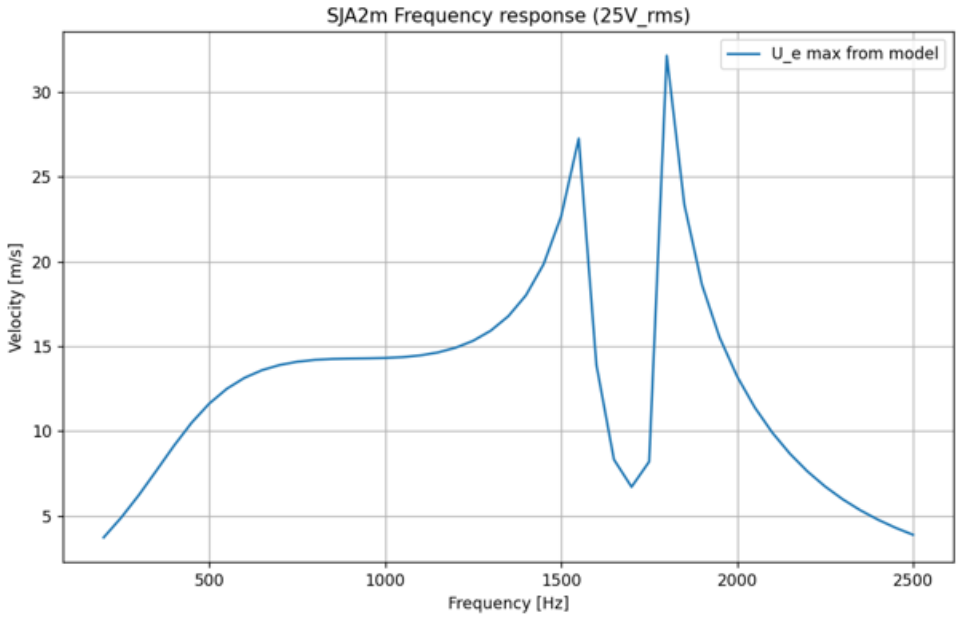

Figure 5.6: Model frequency response for ideal actuation of a Mach 0.5 jet.

Table 5.3 showcases the values of the cavity and orifice geometry resulting in the model response of Figure 5.6.

Parameter Name	Cavity Diameter	Cavity Height	Orifice Diameter	Orifice Length
Value	41mm	1.5mm	1mm	1mm

Table 5.3: Parameter values for the synthetic jet actuator

Note that due to the standardized size of piezoelectric diaphragm, the cavity diameter is fixed at 41mm. Moreover, it was chosen to have $l_0 = d_0$ for the sake of simplicity.

5.3. Actuator Manufacturing & Testing Setup

This section a brief description of the actuator design, manufacturing and testing will take place. Given the ideal geometry found in the previous section, the design was done in Catia with the aim to be 3D

printed.

Design and manufacturing

The design involves a single piece which incorporates the cavity and the orifice with said geometry and a slot in which the piezoelectric element can attach and be glued onto. Precise attachment and gluing is very important to avoid air leakage from the back end of the actuator which would cause a large inefficiency in the synthetic jet creation. Note that the slot has a thickness of 0.5mm which means that the cavity effectively ends up having a slightly suboptimal diameter of 40mm instead of 41mm. An exaggerated sketch of the diametric cross-section of the disk-like actuator is visualised in Figure 5.7.

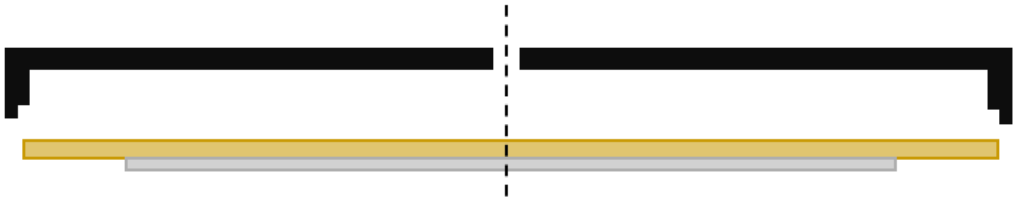

Figure 5.7: Exaggerated cross-section of actuator design showcasing the 3D printed cavity-orifice setup including the slot for the placement of the piezoelectric diaphragm.

With this design, the manufacturing steps become as simple as follows:

- 3D print cavity with required geometry
- Drill orifice for precise dimensions
- Attach and glue piezoelectric element to cavity

These simple steps result in the following actuator of Figure 5.8 as manufactured in the labs of UC3M in Madrid. This design was simply made using CATIA V5 and 3D printed using resin.

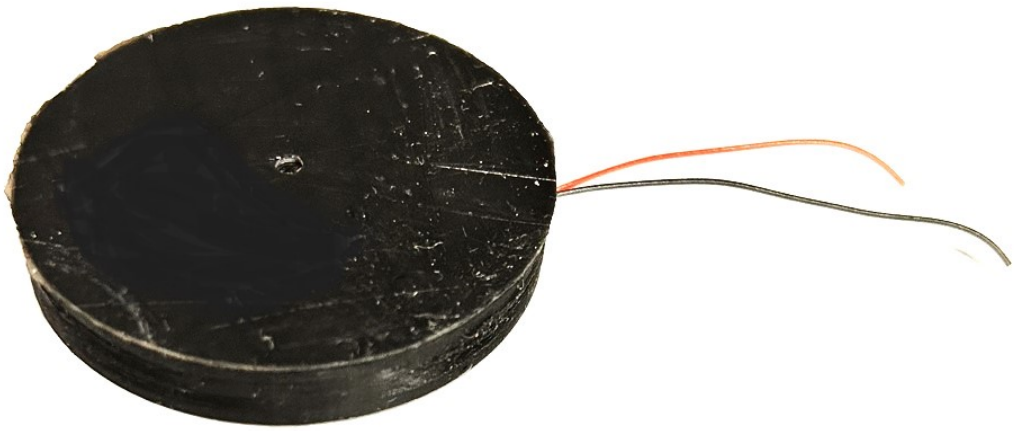

Figure 5.8: Manufactured piezoelectric-driven actuator.

In Figure 5.8 the jet-creating side is shown with the orifice visible on top while the piezoelectric diaphragm (brass sheet attached onto the piezoelectric ceramic) is glued on the other side. The lead wires through which the piezoelectric ceramic is stimulated are shown on the right.

Setup and testing

With regards to the setup of the actuator, the only input is the signal on the lead wires.

The desired signal is designed and controlled using LabVIEW before being fed into a signal generator. From the signal generator the signal passes through an amplifier and is finally connected to the two ends of the piezoelectric element. Both elements are shown in Figure 5.9.

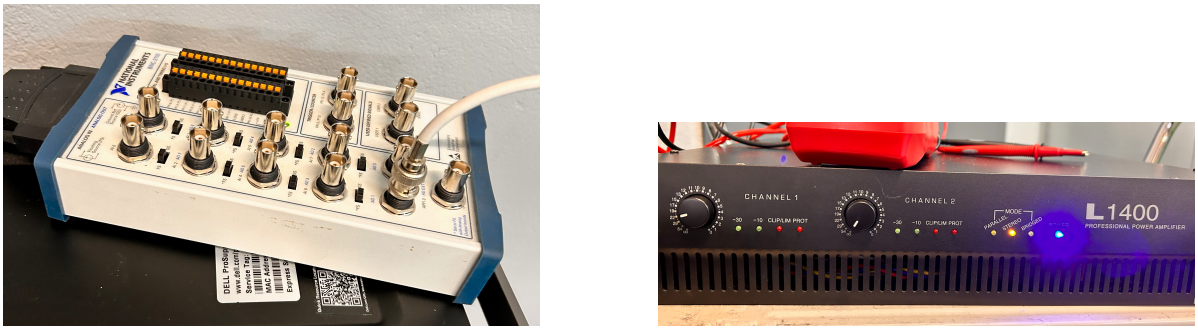

(a) Signal generator **(b)** Amplifier

Figure 5.9: Signal generator and amplifier used for creating and amplifying the signal before feeding it into the actuator ends.

Note that a voltmeter is placed after the amplifier to capture the voltage of the signal.

In this way, the frequency as well as the amplitude of the signal is controlled through the computer, assuming always a sinusoidal signal.

Moving on to the testing, a hot-wire was used to capture the precise velocity right outside of the orifice where the synthetic jet is supposed to act. The standard steps required for this hot-wire test, the same way as described in the thesis by Marin Quintero [36], are presented below:

- **Synthetic Jet Actuator setup:**
  - Securing the actuator: The synthetic jet actuator is securely mounted on a solid platform that can be precisely moved in 2 dimensions to ensure consistent positioning during the test.
  - Signal and power supply: The piezoelectric element is connected to the signal supply as described previously that can control the driving frequency and amplitude on demand.
- **Hot-Wire Anemometer calibration:**
  - Calibration process: A standard calibration of the hot-wire anemometer using King's law is performed using a known reference flow that is provided through a uniform tube with controlable air mass flow. In this case the standard calibration curve is automatically calculated using a software.
  - Anemometer parameters tuning: The anemometer's settings are manually tuned (gain and offset) according to the expected velocity range of the experiment. In this case a maximum expected velocity of 30m/s was considered.
- **Hot-Wire Anemometer positioning:**
  - Vertical alignment: The hot-wire probe is positioned at the desired location relative to the orifice of the synthetic jet actuator. As discussed earlier, in experiments of this kind the probe is placed 1 diameter away from the orifice and this captures the saddle-point velocity.
  - Horizontal alignment: Since the SJA is placed on controlable platforms, the horizontal alignment in both axis is done through precisely adjusting the SJA's location rather than the probe itself. In this way a precise 3-dimensional positioning is achieved.

The full setup is seen below in Figure 5.10 showcasing the movable platforms, the clamped SJA, the connected power and signal supply and the positioned hot-wire anemometer.

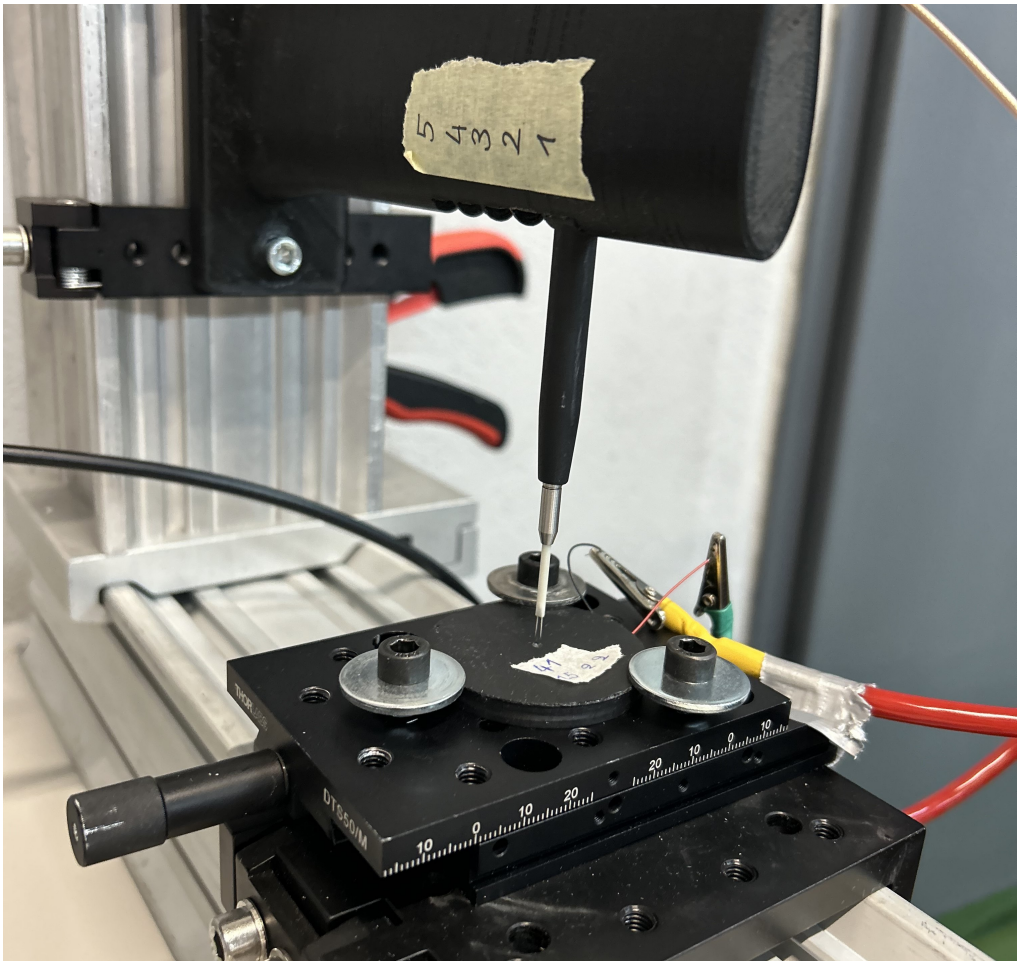

Figure 5.10: Full setup of the SJA with the Hot-Wire for the testing.

A closer look on the clamping of the SJA on the platform and the hot-wire probe placed 1 diameter away from the orifice is given in Figure 5.11.

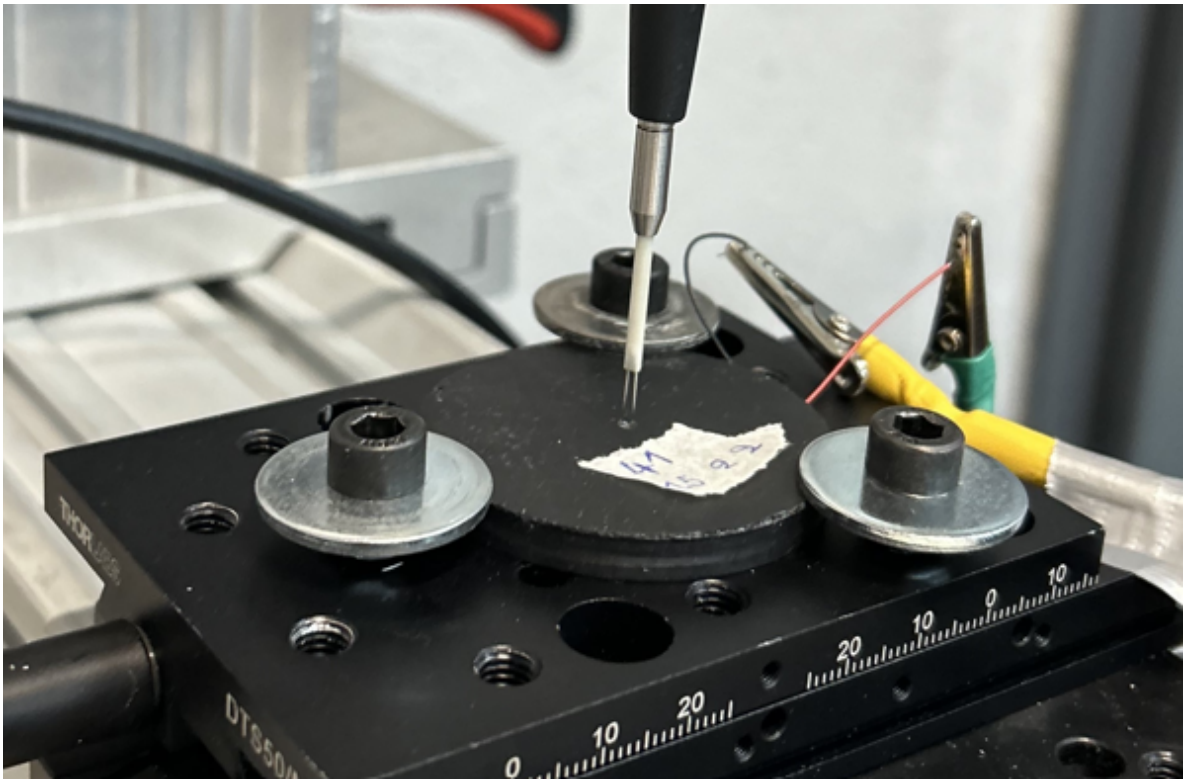

Figure 5.11: Closer view on the setup of the SJA with the Hot-Wire for the testing.

Uncertainties and Equipment Limitations

Throughout the design, manufacturing, and testing phases of the piezoelectric-driven synthetic jet actuator, some sources of uncertainty were identified that could affect the accuracy and reliability of the results.

Firstly, during the 3D printing process, the manufacturing tolerance of the 3D printer was within ± 0.1 mm. Furthermore, the precision of the orifice drilling can also be assumed to be within ± 0.1 mm, ensuring the orifice closely adhered to the desired geometry. However, these tolerances could introduce slight deviations in the actuator's performance due to imperfections in the cavity shape. Another limitation that could add to the uncertainty is the orifice drilling angle. It should be mentioned that the drilling was done with manual alignment which could result in a slight tilt of the orifice. No exact measurement of the tilt was done however it can be safely assumed that it would not exceed 5 degrees. Since the SJAs act a couple of diameters away from the orifice, this slight tilt should not be enough to influence the effective jet injection into the boundary layer.

Moving to the hot-wire anemometer, used to measure the velocity at the orifice, introduced its own uncertainties. During calibration, which was performed according to King's law, the hot-wire anemometer is assumed to have exhibited a velocity measurement uncertainty of no more than $\pm 2\%$. This corresponded to an approximate maximum uncertainty of ± 0.5 m/s in the velocity measurement range (about 0 - 30 m/s). Furthermore, fluctuations in ambient temperature during calibration and testing phases could introduce additional uncertainties which are however assumed to be negligible in this case.

Regarding positioning accuracy, the hot-wire anemometer probe was placed using a movable platform with a high positional accuracy. This ensured that the probe was consistently aligned in the horizontal plane and it is assumed that no significant misalignment can be introduced in this horizontal plane. However, in the vertical direction which defined the distance of the hot-wire thread from the orifice plane, the alignment was done manually with the aim of having a 1 orifice diameter distance. Since no exact measurement was done to ensure that the distance was precisely 1mm, uncertainty was introduced in this part. A safe assumption is that the distance was within 20% from the required one. This last

error could be the only one to introduce significant uncertainty into the final velocity measurement. As seen however in numerical simulations as well as experiments performed to understand the decay of streamwise velocity away from the orifice, it is seen how in the vicinity of the streamwise position of 1 diameter, no significant decay is noted [25, 27]. This can be seen in the phased-average graph of the streamwise velocity for various streamwise locations away from the orifice where the maximum velocity at locations 0.8 and 1.2 diameters away is the same with the only difference being the amount of time this maximum velocity is sustained during one cycle [25].

5.4. Frequency Response Results & Evaluation

The testing of the actuator comprised measurements of the saddle-point velocity by the hot-wire for each frequency of operation of the actuator. Given the expected range of actuation in the frequency spectrum, measurements were performed for the frequencies starting from 200Hz till 2500Hz in increments of 50Hz.

During the measurement at a given frequency of actuator operation, the hot-wire anemometer data would capture readings at an acquisition frequency of 50kHz and the sampling was set to last for 2 seconds resulting in a total of 100k readings per frequency. Note that the acquisition frequency, even though the Nyquist criterion dictates a requirement as low as 5kHz (given that the maximum actuator operation frequency would be around 2.5kHz during the testing) was chosen to be as high as 50kHz to be able to fully capture the actuator exit cycle. Moreover the sampling time was also chosen at 2 seconds in order to capture multiple air ejection-injection cycles and verify the cycle consistency. Below, the analysis of the data is explained and the resulting frequency response is presented and discussed.

5.4.1. Data analysis

A snapshot of the whole 2 second sample of the raw hot-wire data with the actuator operating at 1.5kHz is shown at Figure 5.12.

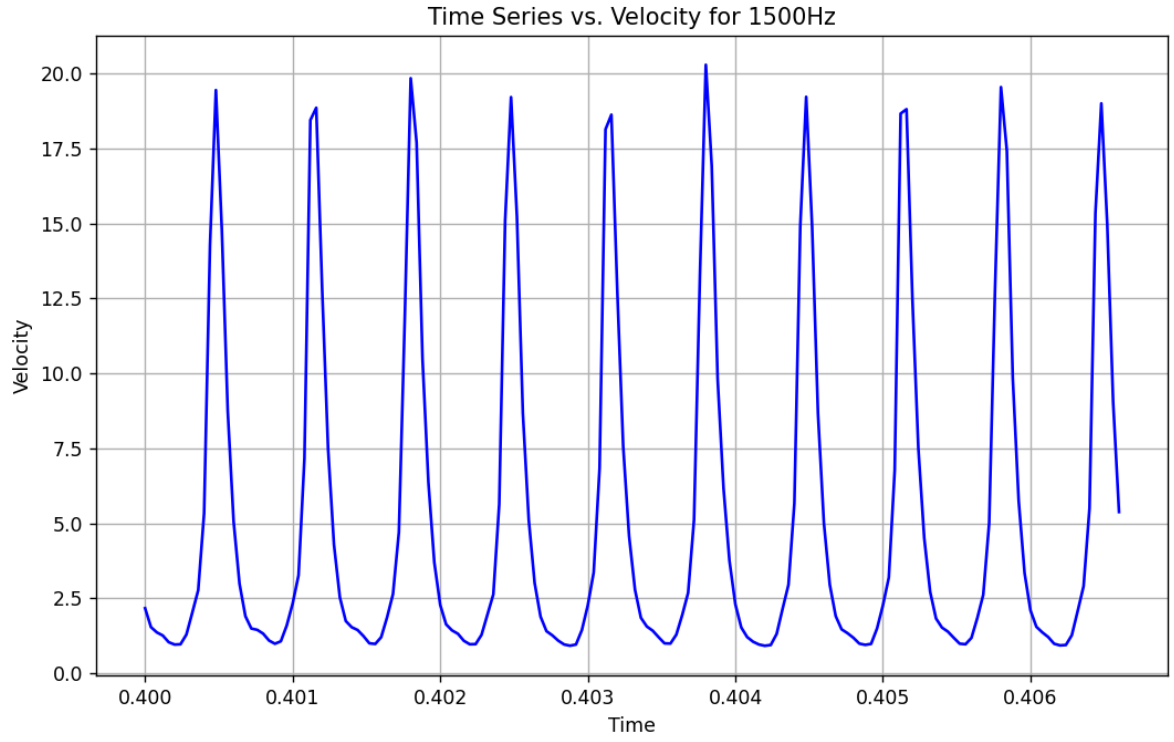

Figure 5.12: Snapshot including the raw hot-wire measurements for 10 cycles at 1.5kHz of actuator operation.

It is seen how the velocity cycles are very consistent and how their frequency indeed corresponds to the

frequency of the signal. For instance, the left-most and right-most peaks of the signal in Figure 5.12 correspond to timestamps 0.40048 and 0.40648 seconds respectively and encapsulate 9 full cycles. This corresponds to $\frac{9}{0.006s} = 1500Hz$ which is precisely the signal frequency.

In order to derive a single value corresponding to the maximum velocity during the oscillation, a windowed-averaging procedure was followed. This involved splitting the whole sample into ”windows” of initially 10 cycles, obtaining the max value for each ”window” and finally averaging over all the max values. This way the computational cost is decreased compared to a phase-averaging technique. Note that a small testing was done where the amount of cycles in each window was used as a variable and results showed that the same max value was given going from a single cycle to even 200 cycles, showing how phase-averaging would yield the same value as more efficient windowed-average computations of the max.

With that in mind, a maximum value of the actuator saddle-point velocity was calculated for each frequency step, resulting in the full frequency response as seen in the blue line of Figure 5.13.

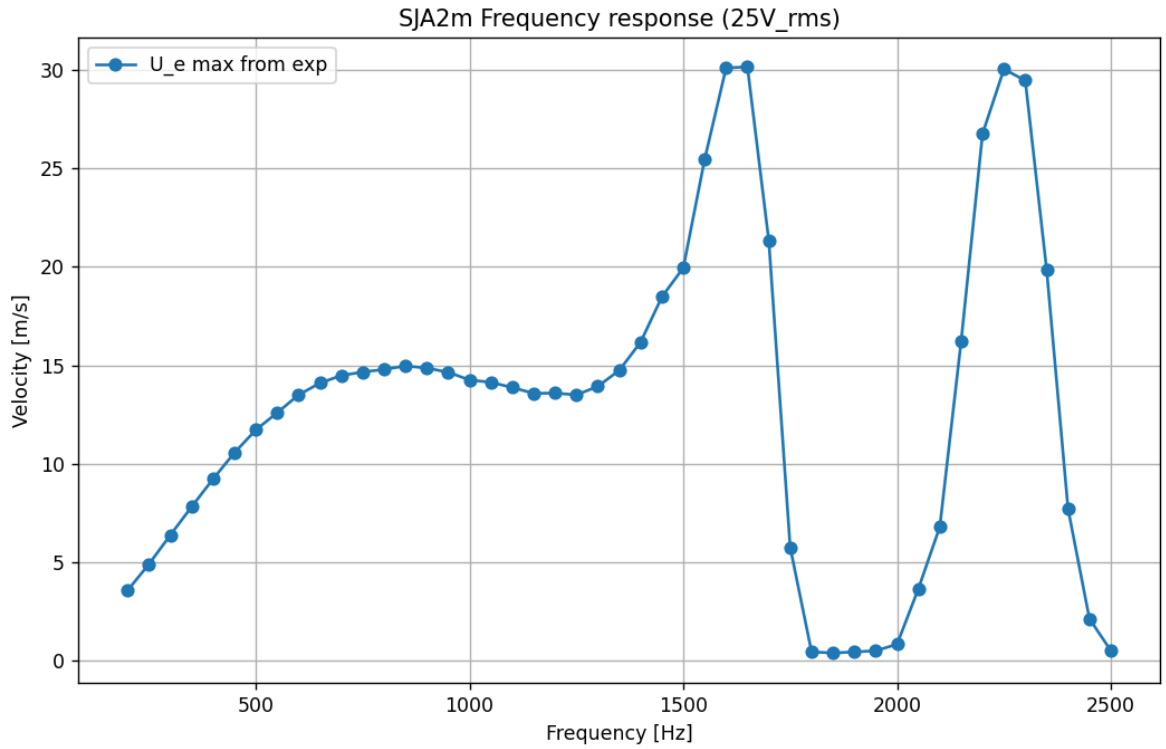

Figure 5.13: Experimental frequency response for actuator SJA2m.

5.4.2. Evaluation

Figure 5.13 showcases an interesting deviation from theory. As discussed in the previous chapter, the modelling of those types of actuators assumes a double coupled resonator system which in turn corresponds to two system resonant frequencies, namely the Helmholtz and the model structural frequency, the coupling of which can vary depending on the actuator. In this case however, three distinct peaks can be seen at 850, 1650 and 2250Hz respectively. After extracting the Helmholtz and the structural frequency as calculated by the model and comparing it to the ones seen by the experiment, a 1 to 1 matching can be done for those two frequencies. The Helmholtz and structural frequency given by the resonator model correspond to 750 and 1700Hz respectively which closely resemble the smooth peak shown around 850Hz and the sharper peak around 1650Hz. This highlights a match between the theory and the experiments however there is still the unexpected third peak to be assessed. After close examination of the characteristics of the piezoelectric diaphragm it was found that the structural

resonant frequency of the diaphragm as given by the manufacturer corresponds to 2300Hz which is extremely close to the 2250Hz of the third peak and thus a matching can be done there as well. The exact diaphragm used is the model 81-7BB-41-2L0 by Murata Electronics with the piezoelectric ceramic attached to the 41mm diameter brass disk. Therefore, the following matching as seen in Table 5.4 is made between the theoretically expected and the experimental resonant frequencies:

	Helmholtz Frequency	**Model Calculated System Structural Frequency**	**Manufacturer Recommended Diaphragm Structural Frequency**
Theoretically Calculated Resonant Frequency	750 Hz	1700 Hz	2200 Hz
	Peak Frequency 1	**Peak Frequency 2**	**Peak Frequency 3**
Experimentally Measured Frequencies	850 Hz	1650 Hz	2250 Hz

Table 5.4: Comparison of Theoretical and Experimental Peak Frequencies

Evaluation of actuator response vs initial requirement

As derived by the performed theoretical modelling and as stated previously, the initial goal was the following:

The actuator should have the capability to provide velocity fluctuations reaching a U_{max} of approximately 15m/s at a frequency ranging from 600 to 800Hz.

After evaluation of the experimental frequency response, one can see how the goal has been met for the most part. Figure 5.14 nicely illustrates how effective the designed actuator is in satisfying the set goal.

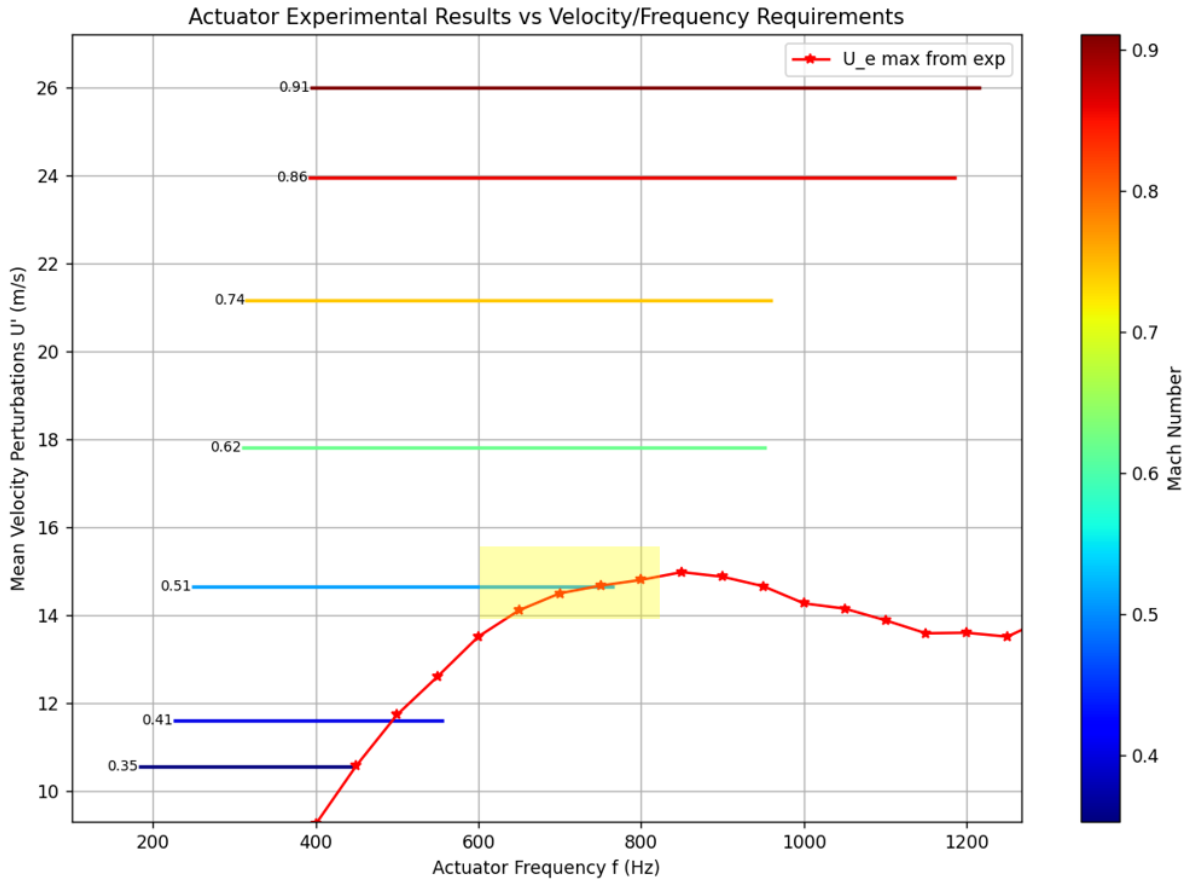

Figure 5.14: Experimental actuator response of actuator SJA2m vs Velocity/Frequency requirement.

It is seen how the velocity requirement is approximately reached and sustained for the frequencies ranging from 700 till 900Hz whereas ideally the range should be 100Hz lower. However, with a change in geometry the Helmholtz resonance frequency would appear at a lower frequency thus meeting the requirement.

Model fitting

Having satisfied the initial energy/frequency requirement in an acceptable range, an assessment of the coupled resonator model is done. Figure 5.15 showcases the experimental frequency response compared with the frequency response as given by the developed model with the manual tuning applied according to the fitting done to another basis geometry.

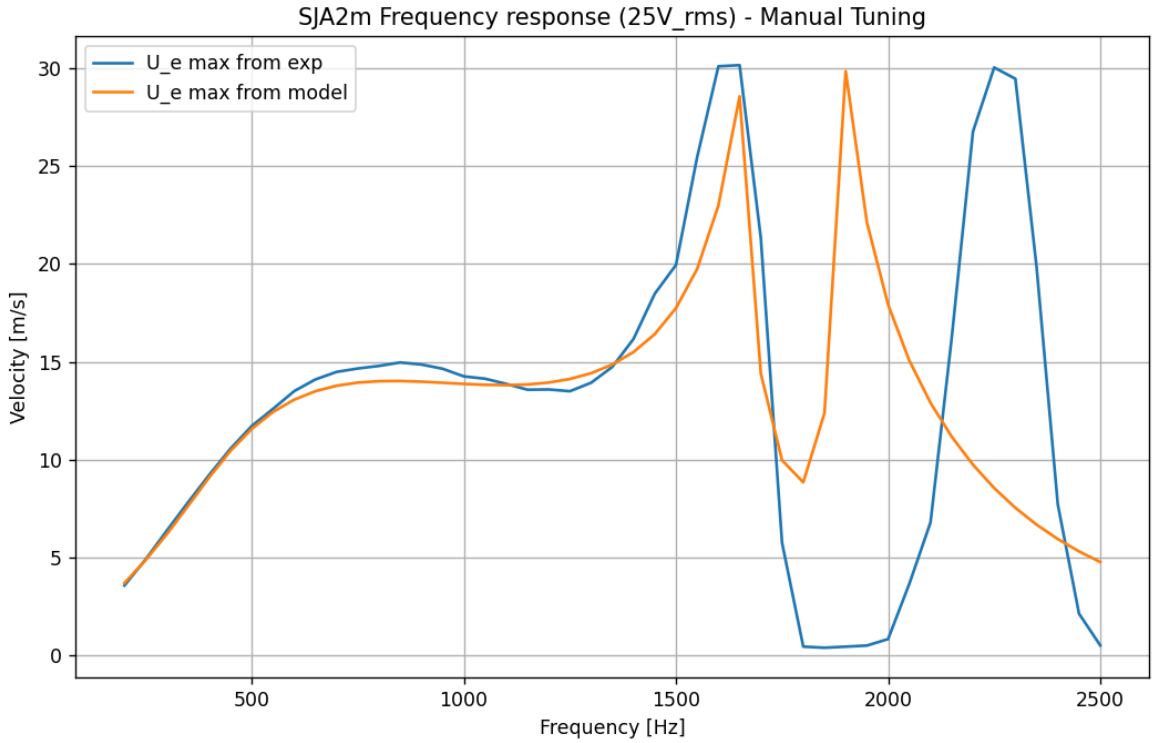

Figure 5.15: Experimental data vs model frequency response for actuator SJA2m.

It is seen how until 1750Hz the response of the model matches the experimental even if there is a small difference of 2m/s at the peak characterised as the model structural frequency. However, after the 1.75kHz mark the model response is shifted approximately 400Hz lower than the experimental frequency response which highlights an inconsistency with the theory. Given that the requirement of this thesis at lower frequencies is satisfied, not much attention is given to this discrepancy which however indicates that more consistent tuning should be done in the future involving the experimental data of a larger number of actuators of this kind. Note that the fact that the larger discrepancy in this case corresponds to the structural frequency as suggested by the manufacturer may be an indication that the model should have the structural frequency of the diaphragm from the manufacturer as a model input which could potentially take the form of a 3rd equation of the coupled system.

Experiment reproducibility

To close off this section, a small verification is presented with regards to the reproducibility of this experiment. In order to verify the consistency if the data collected in the aforementioned experiment, a second experiment was performed. For the sake of efficiency, the same exact experiment was performed however now with twice the step in frequency so as to reduce the experiment time. The results of the 2nd experiment in comparison to the 1st are seen in Figure 5.16.

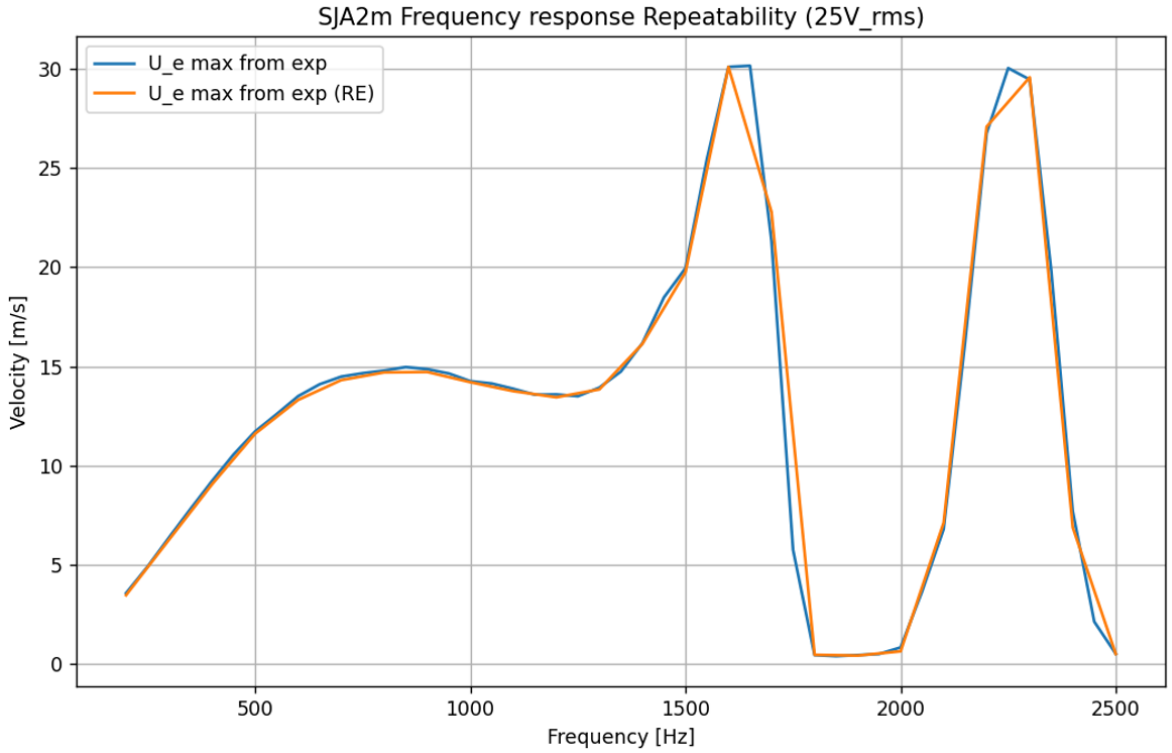

Figure 5.16: Comparison of actuator response after repeating the experiment from scratch. Note that the repeated experiment was done with 100Hz frequency increments.

The 1 to 1 correspondence of max velocities registered for each measured frequency is easily verified and therefore the consistency of the experiment is verified.

6

Conclusions & Recommendations

This thesis has explored the design and application of synthetic jet actuators as a means of reducing jet noise, contributing to the broader goal of aircraft noise mitigation. The research has led to several key conclusions, reflecting both the specific objectives addressed and the more general advancements made in the field of aeroacoustics.

6.1. Equivalence Between Hydrodynamic Structures and Far-Field Noise Emissions in Sub-Sonic Jets

The thesis successfully established an equivalence between the characteristics of hydrodynamic structures and far-field noise emissions in sub-sonic jets. There were several important findings:

- **Predicting Noise-Producing Structures Numerically:** A predictive model was developed, integrating turbulence characteristics with far-field noise data into an iterative optimization algorithm. This model demonstrated a capability to predict the character of noise sources within subsonic jets in the form of energy requirements within a specific frequency range.
- **Frequencies Corresponding to Noise-Producing Structures:** The study identified the most noise-producing structures for a large range of subsonic jets. For each Mach number jet analysed, the frequency range of the most important noise sources was found. For instance in a Mach 0.5 jet the expected noise-sources predominantly occurred within the frequency range of 250 to 800 Hz.
- **Energy Content of Noise-Producing Structures:** The energy content associated with these structures was quantified in terms of kinetic energy which can be translated into velocity fluctuations in the flow with a certain max velocity amplitude. For the case of the Mach 0.5 jet it was found that in the frequency range described before, the noise sources have a specific energy content which corresponds to velocity fluctuations of 15m/s. This energy content then dictates the requirement for effective flow actuation and drives the actuator design later on in the study.

6.2. Construction of Actuators for Energy Output at Specific Frequency Ranges

Another major focus of this research was on constructing actuators capable of delivering the necessary energy output at specific frequency ranges derived from the noise-source prediction model:

- **Effectiveness of Piezoelectric-Driven Synthetic Jet Actuators:** The thesis successfully designed, manufactured, and tested a piezoelectric-driven synthetic jet actuator. This actuator was engineered to meet the specific energy output and frequency requirements needed for effective noise reduction in a Mach 0.5 jet, as outputted by the noise-source prediction model previously. Experimental results confirmed that the actuator performed nearly as expected, delivering the required velocity perturbations within the targeted frequency range, with a slight offset of 100 Hz.

- **Sizing of Actuators Based on Energy/Frequency Requirements:** The research provided a detailed methodology for sizing synthetic jet actuators. This methodology begins by developing a theoretical model for predicting the frequency response of the synthetic jet actuator geometry by modelling it as a coupled system of resonators. The model combines the forcing of the piezoelectric diaphragm together with the vibrational dynamics of the cavity as well as the orifice resulting in an system of coupled differential equations which can be implicitly solved for the velocity response at the exit of the orifice. The theoretical model, coupled with practical design and testing used for tuning specific parameters of the model, led to an optimized actuator geometry capable of meeting the specific energy and frequency requirements.
- **Frequency Response of the Constructed Actuator:** The frequency response of the constructed actuator, as measured by a hot-wire, confirmed that it effectively achieved the desired velocity perturbations, aligning closely with the predicted requirements for noise reduction in sub-sonic jets. For the case of the Mach 0.5 jet, the actuator designed was able to output velocity fluctuations with a max velocity of 15m/s at the frequency range of 700 till 900Hz.

6.3. Recommendations

Building on the conclusions drawn from this study, several personalized recommendations are proposed for future research and practical application:

1. **Expand the Prediction Model:** The prediction model currently relies primarily on farfield data at 90-degree measurements from the jet nozzle. Expanding this model to cover other angles, particularly 20-30 degrees, is recommended due to the directivity that causes a peak in the sound spectrum at these angles. Additionally, optimizing the algorithm used in the noise-source prediction model for more efficient convergence could improve accuracy. It is particularly suggested to consider a greater number of volumes in the flow so as to better characterise the noise spectrum and draw more concrete conclusions about the energy content of the structures with frequencies corresponding to the most noise-producing sources.
2. **Improve and Automate Resonator Model Tuning:** Future experiments should involve testing multiple actuators of this type with varying geometries and derive the tunable parameters to fit all tested actuators, as tuning based on a single actuator may not provide a complete understanding. Furthermore, the resonator model tuning process could be improved by implementing a loss function for automatic tuning, rather than relying on manual adjustments. This could lead to more precise and consistent results across different actuator geometries as well.
3. **Investigate Theory of Resonator System:** The current thesis revealed three peak frequencies after the experimental response, whereas the literature typically reports only two (Helmholtz and structural resonances). Further research should explore different actuator geometries to determine if the third peak is a consistent phenomenon and if it corresponds to a specific physical mechanism, such as a resonance provided by the manufacturer.

6.4. Project Continuation

This thesis with its literature study, modelling and testing contributes to a larger scale project of active flow control for jet noise mitigation. Following, the next steps of the project are outlined:

1. **Integration into Operational Jet Facility:** The next phase of this project should focus on integrating synthetic jet actuators into an operational jet in a test facility. A promising approach is to implement an actuator grid radially around the nozzle, potentially integrating around six synthetic jet actuators into the nozzle skeleton with the orifice being flush-mounted with the nozzle skin and able to provide the velocity fluctuations in the boundary layer. This configuration would then allow for the development of a control algorithm tailored to the actuator capabilities and positions. The design should include making precise holes on the side of the nozzle to accommodate the actuators, following similar methodologies as seen in recent studies [37].
2. **Long-Term Testing Under Realistic Conditions:** Long-term testing of synthetic jet actuators under realistic operating conditions is recommended. Noise measurements should be taken in the far-field, approximately 72 diameters away, to verify the effectiveness of the noise reduction

strategies under real-world conditions. The testing should be done in an anechoic chamber such as the one designed in the facilities of UC3M in Leganes.

3. **Focus on Control Strategy Development:** Given the actuator capabilities, it is crucial to collaborate with control engineers to develop a control strategy that maximizes noise reduction. Integrating advanced control methods, such as those involving artificial intelligence or real-time reactive control, could significantly enhance the effectiveness of the noise mitigation system [54, 5].

In conclusion, this thesis lays a strong foundation for future research in jet aeroacoustics and active flow control. Future projects should aim to refine the models and technologies developed here based on the given recommendations and other innovative approaches expected to be revealed along the way. This research has opened new avenues for the practical application of synthetic jet actuators in noise mitigation, contributing valuable insights into the broader challenge of reducing environmental noise pollution from aircraft.

References

[1] Brès G. A. et al. “Importance of the Nozzle-Exit Boundary-Layer State in Subsonic Turbulent Jets”. In: *Journal of Fluid Mechanics* 851 (2018), pp. 83–124. DOI: 10.1017/jfm.2018.476.

[2] Faranosov G. A. “A Theoretical Study of the Efficiency of Instability Wave Excitation in a Two-Dimensional Nozzle Edge Model”. In: *Acoustical Physics* 58.4 (2012). Original Russian Text published in Akusticheskii Zhurnal, pp. 503–509. DOI: 10.1134/S1063771012040069.

[3] Glezer A. and Amitay M. “Synthetic Jets”. In: *Annual Review of Fluid Mechanics* 34.1 (2002), pp. 503–529. DOI: 10.1146/annurev.fluid.34.090501.094913.

[4] Hirschberg A. and Rienstra S.W. *An Introduction to Aeroacoustics*. Dept. of Applied Physics and Dept. of Mathematics and Computer Science. Eindhoven, The Netherlands, 2004.

[5] Maia I. A. et al. “Real-time reactive control of stochastic disturbances in forced turbulent jets”. In: *Physical Review Fluids* 6 (2021), p. 123901. DOI: 10.1103/PhysRevFluids.6.123901.

[6] Michalke A. “Survey on jet instability theory”. In: *Progress in Aerospace Sciences* 21 (1984), pp. 159–199. ISSN: 0376-0421. DOI: https://doi.org/10.1016/0376-0421(84)90005-8. URL: https://www.sciencedirect.com/science/article/pii/0376042184900058.

[7] Towne A., Schmidt O. T., and Colonius T. “Spectral proper orthogonal decomposition and its relationship to dynamic mode decomposition and resolvent analysis”. In: *Journal of Fluid Mechanics* 847 (2018), pp. 821–867. DOI: 10.1017/jfm.2018.283.

[8] Freund J. B. “Noise sources in a low Reynolds number turbulent jet at Mach 0.9”. In: *Journal of Fluid Mechanics* 438 (2001), pp. 277–305. DOI: 10.1017/S0022112001004414.

[9] Pope S. B. *Turbulent Flows*. Cambridge University Press, 2000.

[10] Jr. Campbell J. S. et al. “Thermal Management of a Laptop Computer with Synthetic Air Microjets”. In: *1998 Intersociety Conference on Thermal Phenomena*. Boeing North American, Aircraft, Missile Systems Division, and Georgia Institute of Technology, Woodruff School of Mechanical Engineering. Duluth, CA, 1998.

[11] Goldstein M. E. *Aeroacoustics*. Advanced book program. McGraw-Hill International Book Company, 1976. ISBN: 9780070236851. URL: https://books.google.es/books?id=HY1TAAAAMAAJ.

[12] Martini E., Cavalieri A. V. G., and Jordan P. “Acoustic Modes in Jet and Wake Stability”. In: *Journal of Fluid Mechanics* 867 (2019), pp. 804–834. DOI: 10.1017/jfm.2019.148.

[13] Kopiev V. F. et al. “Active Control of Jet–Wing Interaction Noise Using Plasma Actuators in a Narrow Frequency Band”. In: *Acoustical Physics* 69.2 (2023), pp. 193–205. DOI: 10.1134/S1063771022600668.

[14] Kopiev V. F. et al. “Control of Instability Waves in an Unexcited Turbulent Jet Using Plasma Actuators in a Narrow Frequency Band”. In: *Acoustical Physics* 67.4 (2021), pp. 413–420. DOI: 10.1134/S1063771021040059.

[15] Cavalieri A. V. G., Jordan P., and Lesshafft L. “Wave-Packet Models for Jet Dynamics and Sound Radiation”. In: *Applied Mechanics Reviews* 71.2 (2019), p. 020802. DOI: 10.1115/1.4042736.

[16] Ceglia G. et al. “Flow Characterization of an Array of Finite-Span Synthetic Jets in Quiescent Ambient”. In: *Experimental Thermal and Fluid Science* 119 (2020), p. 110208. DOI: 10.1016/j.expthermflusci.2020.110208.

[17] Zong H. et al. “Plasma Synthetic Jet Actuators for Active Flow Control”. In: *Actuators* 7.4 (2018), p. 77. DOI: 10.3390/act7040077.

[18] Lighthill M. J. “Jet Noise”. In: *AIAA Journal* 1.7 (1963), pp. 1507–1517.

[19] Lighthill M. J. “On sound generated aerodynamically - I. General theory”. In: *Royal Society of London Proceedings Series A* 211 (1952), pp. 564–587.

[20] Lighthill M. J. “On sound generated aerodynamically - II. Turbulence as a source of sound”. In: *Royal Society of London Proceedings Series A* 222 (1953), pp. 1–32.

[21] Morris P. J. and Farassat F. “Acoustic Analogy and Alternative Theories for Jet Noise Prediction”. In: *AIAA Journal* 40.4 (2002), pp. 671–680.

[22] Ahuja K. K. and Bushell K. W. “An experimental study of subsonic jet noise and comparison with theory”. In: *Journal of Sound and Vibration* 30.3 (1973), pp. 317–341.

[23] Tanna H. K., Dean P. D., and Burrin R. H. *The Generation and Radiation of Supersonic Jet Noise. Vol. III, Turbulent Mixing Noise Data*. Tech. rep. AFAPL-TR-76-65-Vol. 3. Wright-Patterson AFB, OH: U.S. Air Force Aero-Propulsion Lab., 1976.

[24] Viswanathan K. “Investigation of Noise Source Mechanisms in Subsonic Jets”. In: *AIAA Journal* 46.8 (2008), pp. 2020–2028. DOI: 10.2514/1.34471.

[25] Barton L. and Glezer A. “The formation and evolution of synthetic jets”. In: *Physics of Fluids* 10.9 (Sept. 1998), pp. 2281–2297. ISSN: 1070-6631. DOI: 10.1063/1.869828. eprint: https://pubs.aip.org/aip/pof/article-pdf/10/9/2281/19313524/2281_1_online.pdf. URL: https://doi.org/10.1063/1.869828.

[26] Huff D. L. and Envia E. *Jet Engine Noise Generation, Prediction and Control*. Preprint E-14866. NASA Glenn Research Center, Sept. 2004. URL: https://ntrs.nasa.gov/citations/20050198876.

[27] Kral L. et al. “Numerical simulation of synthetic jet actuators”. In: *4th shear flow control conference*. 1997, p. 1824.

[28] Rego L. F. L. “Aeroacoustics of Jet-Surface Interaction and Passive Solutions for Mitigating Jet-Installation Noise”. Available at http://repository.tudelft.nl/. PhD thesis. Delft, Netherlands: Delft University of Technology, Sept. 2022. DOI: 10.4233/uuid:a50e3a9c-af3a-4e4f-836c-80f70c75847c.

[29] Zhang L. et al. “Effects of Loudspeaker-Driven Synthetic Jet Actuator Parameters on the Characteristics of the Synthetic Jet”. In: *Applied Acoustics* 197 (2022), p. 108943. DOI: 10.1016/j.apacoust.2022.108943.

[30] Zhang L. et al. “Effects of Piezoelectric-Driven Synthetic Jet Actuator Parameters on the Synthetic Jet Formation Process and Actuator Performance”. In: *International Journal of Non-Linear Mechanics* 157 (2023), p. 104561. DOI: 10.1016/j.ijnonlinmec.2023.104561.

[31] de Luca L., Girfoglio M., and Coppola G. “Modeling and Experimental Validation of the Frequency Response of Synthetic Jet Actuators”. In: *AIAA Journal* 52.8 (2014), pp. 1733–1744. DOI: 10.2514/1.J052674.

[32] Basner M. and McGuire S. “WHO Environmental Noise Guidelines for the European Region: A Systematic Review on Environmental Noise and Effects on Sleep”. In: *International Journal of Environmental Research and Public Health* 15.3 (2018). ISSN: 1660-4601. DOI: 10.3390/ijerph15030519. URL: https://www.mdpi.com/1660-4601/15/3/519.

[33] Chiatto M., Palumbo A., and de Luca L. “Design Approach to Predict Synthetic Jet Formation and Resonance Amplifications”. In: *Experimental Thermal and Fluid Science* 107 (2019), pp. 79–87. DOI: 10.1016/j.expthermflusci.2019.05.013.

[34] Chiatto M. et al. “LEM Characterization of Synthetic Jet Actuators Driven by Piezoelectric Element: A Review”. In: *Sensors* 17 (2017), p. 1216. DOI: 10.3390/s17061216.

[35] Ja’fari M., Shojae F. J., and Jaworski A. J. “Synthetic jet actuators: Overview and applications”. In: *International Journal of Thermofluids* 20 (2023), p. 100438. ISSN: 2666-2027. DOI: https://doi.org/10.1016/j.ijft.2023.100438. URL: https://www.sciencedirect.com/science/article/pii/S2666202723001544.

[36] Quintero J. S. M. *Experimental Analysis Of A Synthetic Jet Actuator Under Different Configurations*. Undergraduate Final Project. Bogota, Colombia: Universidad De Los Andes, School of Engineering, Mechanical Engineering Department, 2017.

[37] Reumschüssel J. M. et al. “Experimental jet control with Bayesian optimization and persistent data topology”. In: *Preprint at arXiv* 2405.02020.v1 (May 2024), pp. 1–13. DOI: 10.2514/6.2024-1356. arXiv: 2405.02020 [physics.flu-dyn].

[38] Cattafesta L. N. and Sheplak M. “Actuators for Active Flow Control”. In: *Annual Review of Fluid Mechanics* 43.1 (2011), pp. 247–272. DOI: 10.1146/annurev-fluid-122109-160634.

[39] Dickson N. *ICAO Symposium on Aviation and Climate Change, ”Destination Green”*. ICAO Headquarters, Montréal, Canada. 14-16. May 2013.

[40] Sharma R. N. “Fluid-Dynamics-Based Analytical Model for Synthetic Jet Actuation”. In: *AIAA Journal* 45.8 (2007), pp. 1841–1853. DOI: 10.2514/1.25427.

[41] Bychkov O. et al. “Two Approaches to Modeling the Noise of Low-Speed Subsonic Jets”. In: *Doklady Physics* 67.9 (2022), pp. 269–277. DOI: 10.1134/S102833582209004X.

[42] Gil P. and Strzelczyk P. “Performance and efficiency of loudspeaker driven synthetic jet actuator”. In: *Experimental Thermal and Fluid Science* 76 (2016), pp. 163–174. DOI: 10.1016/j.expthermflusci.2016.03.020.

[43] Jordan P. and Colonius T. “Wave Packets and Turbulent Jet Noise”. In: *Annual Review of Fluid Mechanics* 45 (2013), pp. 173–195. DOI: 10.1146/annurev-fluid-011212-140756.

[44] Holman R. et al. “Formation Criterion for Synthetic Jets”. In: *AIAA Journal* 43.10 (2005), pp. 2110–2115.

[45] Proença A. R. “Aeroacoustics of Isolated and Installed Jets under Static and In-Flight Conditions”. Ph.D. Thesis. Southampton, United Kingdom: University of Southampton, Mar. 2018.

[46] Ginevsky A. S., Vlasov V., and Karavosov R. K. *Acoustic Control of Turbulent Jets*. Berlin, Germany: Springer-Verlag Berlin Heidelberg, 2004. DOI: 10.1007/978-3-540-39914-8.

[47] Liu S., Meneveau C., and Katz J. “On the properties of similarity subgrid-scale models as deduced from measurements in a turbulent jet”. In: *Journal of Fluid Mechanics* 275 (1994), pp. 83–119.

[48] Rienstra S.W. and Hirschberg A. *An Introduction to Acoustics*. Extended and revised edition of IWDE 92-06. Eindhoven University of Technology, 2021.

[49] Suzuki T. “A review of diagnostic studies on jet-noise sources and generation mechanisms of subsonically convecting jets”. In: *Fluid Dynamics Research* 42 (2010), p. 014001. DOI: 10.1088/0169-5983/42/1/014001.

[50] Belyaev I. V. et al. “Development of the Strategy of Active Control of Instability Waves in Unexcited Turbulent Jets”. In: *Fluid Dynamics* 53.3 (2018). Original Russian Text published in Izvestiya Rossiiskoi Akademii Nauk, Mekhanika Zhidkosti i Gaza, pp. 347–360. DOI: 10.1134/S0015462818030047.

[51] Tam C. K. W. “Jet Noise: Since 1952”. In: *Theoretical and Computational Fluid Dynamics* 10 (1998), pp. 393–405. DOI: 10.1007/BF00311867.

[52] Tam C. K. W. and Hu F. Q. “On the three families of instability waves of high-speed jets”. In: *Journal of Fluid Mechanics* 201 (1989), pp. 447–483. DOI: 10.1017/S002211208900100X.

[53] Tam C. K. W. et al. “The sources of jet noise: experimental evidence”. In: *Journal of Fluid Mechanics* 615 (2008), pp. 253–292. DOI: 10.1017/S0022112008003704.

[54] Zhou Y. et al. “Artificial intelligence control of a turbulent jet”. In: *Journal of Fluid Mechanics* 897 (2020), A27. DOI: 10.1017/jfm.2020.392.

[55] Zhang Z. and Wu X. “A unified theory for the envelope radiation of ring-mode coherent structures in the very-near-nozzle and developed regions of a circular jet”. In: *Physics of Fluids* 35 (2023), p. 014113. DOI: 10.1063/5.0134063.